

Exoplanets in reflected starlight with dual-field interferometry

A case for shorter wavelengths and a fifth Unit Telescope at VLTI/Paranal

S. Lacour^{1,2}, Ó. Carrión-González¹, and M. Nowak^{3,4}

¹ LESIA, Observatoire de Paris, PSL, CNRS, Sorbonne Université, Université de Paris, 5 place Janssen, 92195 Meudon, France

² European Southern Observatory, Karl-Schwarzschild-Straße 2, 85748 Garching, Germany

³ Kavli Institute for Cosmology, University of Cambridge, Madingley Road, Cambridge CB3 0HA, United-Kingdom

⁴ Institute of Astronomy, University of Cambridge, Madingley Road, Cambridge CB3 0HA, United-Kingdom

Received September 15, 1996; accepted March 16, 1997

ABSTRACT

Context. The direct observation of cold and temperate planets within 1 to 10 AU would be extremely valuable for uncovering their atmospheric compositions but remains a formidable challenge with current astronomical methods. Ground-based optical interferometry, capable of high angular-resolution imaging, offers a promising avenue for studying these exoplanets, complementing space-based observations.

Aims. Our objective is to explore the fundamental limits of dual-field interferometry and assess its potential for characterizing exoplanets in reflected light using the Very Large Telescope Interferometer (VLTI).

Methods. We developed analytical expressions to describe the performance of dual-field interferometry and integrated these with simulations of atmospheric wavefronts corrected by extreme Adaptive Optics. An analytical solution for optimal phase apodization was formulated to enhance starlight rejection when injected into a single-mode fibre. This framework was applied to determine the detectability of known exoplanets in reflected light across various wavelength bands for both the current VLTI and a proposed extended version.

Results. Our results indicate that employing shorter wavelengths improves detectability, enabling at least seven Jupiter-mass exoplanets to be observed in the J band with current VLTI's baselines. Adding new baselines with lengths beyond 200 meters significantly enhances VLTI's capabilities, increasing the number of detectable exoplanets and revealing potential habitable zone candidates such as τ Ceti e and Proxima Centauri b.

Conclusions. To substantially improve the VLTI's exoplanet characterization capabilities, we recommend developing instrumentation at wavelengths shorter than $1 \mu\text{m}$, as well as the addition of a fifth Unit Telescope (UT5).

Key words. Planets and satellites: fundamental parameters — planets and satellites: terrestrial planets — planets and satellites: gaseous planets — Astronomical instrumentation, methods and techniques — Techniques: high angular resolution — Techniques: interferometers

1. Introduction

Over the past two decades, direct-imaging has become a key method for the characterization of exoplanets. Its development is now a priority within the community, as illustrated by key community reports and space agencies (Astro 2020 Decadal Survey, and ESA's Voyage 2050 Senior Committee report, for example). Direct-imaging has a particular role to play as it can overcome some of the main limitations of other methods. For example, observing molecular (bio)signatures via transit spectroscopy can be made extremely challenging by the fact that these molecules are often concentrated in lower atmospheric layers (Lustig-Yaeger et al. 2019). Consequently, several direct-imaging space observatories have been proposed, and are under study. The Coronagraph Instrument on the Nancy Grace Roman Space Telescope (Spergel et al. 2015) is poised to be the first to directly image exoplanets in reflected light, from space. Future flagship missions, like the Habitable Worlds Observatory, are being conceptualized based on the LUVOIR (The LUVOIR Team 2018) and HabEx (Mennesson et al. 2016; Gaudi et al. 2018) studies. In Europe, momentum is building for the LIFE project (Quanz et al. 2021), a mid-infrared optical interferometer targeting thermal emission.

Compared to their space-based counterparts, ground-based observatories offer distinct advantages, with usually much larger apertures and higher angular resolution, but also specific challenges, such as an important thermal background and atmospheric aberrations. Several young massive exoplanets have already been successfully discovered and directly imaged from the ground. These are usually hot planets, such as β Pictoris b (approximately 1700 K) and 51 Eri b (around 800 K) which are still cooling off by gradually dissipating the gravitational energy accumulated during their formation. Their thermal emission is comparatively bright against their host stars, with contrast ratios on the order of a few 10^{-5} . But the vast majority of planets are older and colder than these young giants, with a temperature set by the radiative equilibrium with their stellar hosts. Such bodies primarily emit in the mid-infrared wavelength range. To be detected in the near-infrared, these objects must be observed in reflected light, typically at a contrast on the order of 10^{-7} or lower, depending on their radius, semi-major axis, phase angle and albedo.

Given the challenges associated with achieving sufficient contrast levels, the question arises: can exoplanets be effectively characterized in reflected light from ground-based ob-

servatories? Guyon (2005) provides a comprehensive overview of the challenges involved. The first major challenge is atmospheric perturbations, which can be mitigated in single-dish telescopes using Adaptive Optics (AO) systems, such as the Spectro-Polarimetric High-contrast Exoplanet REsearch (SPHERE) extreme AO (Beuzit et al. 2019). The second challenge involves the diffraction pattern, which generates photon noise at the location of the planet; this issue can be addressed with the use of a coronagraph (Rouan et al. 2000). The third, and perhaps most significant challenge, involves non-common path quasi-static aberrations that produce slowly moving speckles, difficult to calibrate. These speckles, with intensities around 10^{-5} , require stabilization to within 1%, necessitating a wavefront stability of 4 pm (Guyon 2005).

These quasi-static speckles can be subtracted using advanced post-processing techniques such as Spectral Differential Imaging (SDI Racine et al. 1999) and Angular Differential Imaging (ADI Marois et al. 2006), or in real time through focal plane wavefront sensing and correction methods like the dark-hole method (Potier et al. 2022). However, these methods require that the wavefront remains stable throughout the observation period; otherwise, shifting speckles cannot be accurately removed. This stringent requirement for temporal stability has spurred the development of new techniques that utilize high-resolution spectral signatures detectable through cross-correlation techniques (Snellen et al. 2013, 2015). Such techniques are seen as powerful tools for the first generation of Extremely Large Telescope (ELT) instruments, including MICADO, HARMONI, and ANDES, which leverage the substantial photon counts captured by the ELT (Palle et al. 2023). Unfortunately, these techniques are limited to detecting targets with strong molecular absorption bands and are ineffective at seeing smooth emission, thus failing to probe continuum albedos or detect exoplanets lacking a dense atmosphere.

In this context, optical interferometry offers a complementary alternative, as its post-processing does not rely on any spectral feature. Several high-contrast interferometric designs exist, generally classified into two main types: single-field and dual-field interferometers. Single-field interferometry differentiates the coherent signals of stars and exoplanets using techniques such as closure phase (Gardner et al. 2018), nulling (Bracewell 1978), or a combination of these methods, such as Kernel nulling (Martinache & Ireland 2018; Chingaipe et al. 2023). Dual-field interferometry, as summarized in Fig. 1, operates by simultaneously observing two narrow fields of view — typically the size of the telescope's point spread function — situated within a larger field of view that can include both a star and an exoplanet. This configuration allows one interferometer to focus on the star while the other targets the exoplanet, minimizing the contamination of the exoplanet signal by stellar photon noise due to the narrowness of each telescope's diffraction pattern.

The GRAVITY instrument (Gravity Collaboration et al. 2017) at the Very Large Telescope Interferometer (VLTI) has pioneered dual-field interferometry, and was incidentally the first interferometer to directly detect an exoplanet (GRAVITY Collaboration et al. 2019). It has also provided the first direct detection of two short-separation radial-velocities exoplanets: β Pictoris c (Nowak et al. 2020) and HD 206893 c (Hinkley et al. 2023). These two planets have not been directly observed by any other instrument to date, suggesting that dual-field interferometry is performing better than imaging at such small separations. The commissioning of GRAVITY+ will bring extreme AO to all the Unit Telescopes (UTs) which, coupled with dual-field interferometry (Gravity+ Collaboration et al. 2022), will further in-

crease this capability and optimize the VLTI for high-contrast (Pourré et al. 2024).

These developments prompt an inquiry into the fundamental limits of dual-field interferometry and its potential to detect exoplanets using reflected light from the ground. In Section 2, we introduce a detailed analytical model to assess the performance and limitations of dual-field interferometry using the existing VLTI. Because photon noise is a prime limitation, Section 2.5 presents a novel, semi-analytical method for determining the optimal phase apodizer necessary for starlight suppression when channeling light into a single-mode fibre. Section 3 suggests a possible upgrade of the VLTI, in which a new 8 m Unit Telescope (UT5) would be added to optimize the VLTI for exoplanet detection, by creating four additional baselines in the 200 m regime to the North-West direction. In Section 4, we estimate the number of known Radial Velocity (RV) exoplanets that could potentially be characterized by the VLTI, including UT5 or not. Finally, Section 5 highlights the main results of this paper.

2. Simulation of Contrast Range

2.1. The Detection Principle

A concise overview of the working principle of a dual-field optical interferometer used for high-contrast exoplanet observations is given in Fig. 1. This setup involves splitting light from two telescopes into four focal planes, in which single-mode fibres are placed. Two fibres, which feed a first interferometer, are centred on the geometrical image of the star, whereas the other two fibres, which feed a second interferometer, are centred on the geometrical image of the planet. A dedicated metrology system monitors the non-common optical-path differences between the two interferometers.

The detection principle relies on the premise that the exoplanet's location is already known, with a precision well within the field of view of the single mode fibres (≈ 60 mas for an 8 m telescope in the K band). This implies that this method is more suited for characterizing exoplanets (for example, measuring their albedo) rather than discovering new ones.

Given the typical planet to star contrast ratio (at least 10^{-4} , and usually much smaller), the first interferometer I_1 is always dominated by photons from the star, while the second interferometer I_2 receives both the photons from the planet, and some non-negligible amount of residual starlight. The light from the planet and the light from the star being fully incoherent, this results in two superimposed systems of fringes observed in the second interferometer.

Separating these two systems of fringes observed on interferometer I_2 to recover the planet coherent flux is one of the main concern of high-contrast dual-field interferometry. For this, two strategies are used in combination: (1) minimizing the amount of starlight entering the fibres feeding interferometer I_2 in the first place (a process thereafter referred to as "apodization"); (2) separating the two fringe systems in post-processing, by taking advantage of the fact that the on-axis starlight and the off-axis planet light creates fringes centred at different Optical Path Difference (OPD) values.

2.2. Spelling out the electric fields

In the next sections of this paper, we will use the symbol \star in subscript to denote parameters associated with the star, and we will use \bullet for those associated with the planet. We denote α the vector representing the angular separation between the star and

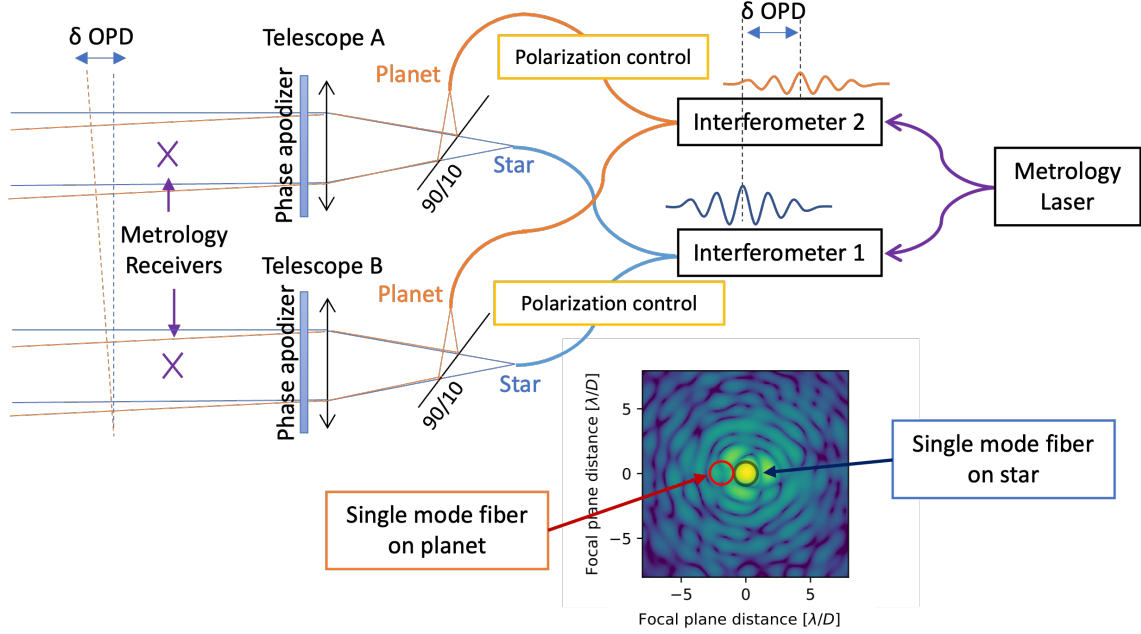


Fig. 1. Schematic diagram of a dual field optical interferometer using two telescopes. A beam splitter creates two images of the focal plane, where two fibres are positioned—one on the star to feed Interferometer 1 (serving as the phase reference) and the other on the exoplanet, feeding Interferometer 2. The exoplanet is detected as coherent flux in Interferometer 2, with a phase offset relative to the stellar coherent flux due to an optical path delay δOPD , corresponding to the scalar product of the narrow angle baseline vector \mathbf{B} and the angular separation between the star and exoplanet α : $\delta\text{OPD} = \alpha \cdot \mathbf{B}$.

the exoplanet: $\alpha = \alpha_{\bullet} - \alpha_{\star}$, where α_{\bullet} points towards the planet, and α_{\star} points towards the star.

We model the interferometric setup using two independent 8 m telescopes, with pupil shapes akin to those of a UT of the VLT. We assume that these telescopes are equipped with an AO system which corrects for the atmospheric turbulence, and we denote $\Phi(\mathbf{u})$ the phase residuals downstream of the AO on the pupil of a given telescope. A term $\Psi(\mathbf{u})$ will also be added at the beginning of section 2.5 to include a pupil phase apodizer. The two-dimensional vector \mathbf{u} is the X-Y coordinate vector within the telescope's pupil. The narrow-angle baseline, the vector between the two telescopes (the vector delimited by the metrology, as outlined by Woillez & Lacour 2013), is denoted as \mathbf{B} .

With this setup, a monochromatic point source of wavevector $k = 2\pi/\lambda$ located at a vector position α on the sky and radiating on the telescope with a flux $F = A^2$, generates an electric field within the pupil of a given telescope which can be described by:

$$W(\mathbf{u}) = A e^{-ik\alpha \cdot \mathbf{u} + i\Phi(\mathbf{u})}. \quad (1)$$

The flux entering a single-mode fibre is determined by projecting the electric field onto the fibre's fundamental mode. This can be calculated either in the focal plane or in the pupil plane, leveraging the Parseval-Plancherel theorem and assuming the far-field Fraunhofer condition. Using the pupil-plane approach, the electric field from Eq. (1) couples into a single-mode fibre as follows:

$$E = \iint_D A e^{-ik\alpha \cdot \mathbf{u} + i\Phi(\mathbf{u})} M^*(\mathbf{u}) d\mathbf{u}, \quad (2)$$

where the integral covers the pupil area with diameter D . The fibre's fundamental mode, represented in the pupil plane as $M(\mathbf{u})$, can be approximated by a Gaussian-shaped mode with beam

waist w :

$$M(\mathbf{u}) \propto \exp\left(-\frac{|\mathbf{u}|^2}{2w^2}\right), \quad (3)$$

where a normalization factor must be added to ensure the conservation of energy. For a circular aperture telescope without central obstruction, optimal injection is achieved with $w = \sqrt{0.1} D$ and $M(\mathbf{u})$ can be exactly spelled as:

$$M(\mathbf{u}) = \frac{2}{\sqrt{0.1}\pi D^2} \exp\left(-\frac{|\mathbf{u}|^2}{0.2D^2}\right), \quad (4)$$

leading to the optimal throughput in the absence of phase aberrations: $\left\| \iint_D M(\mathbf{u}) d\mathbf{u} \right\|^2 = 0.81$.

This expression of $M(\mathbf{u})$ is valid for a fibre located at the focal point of the telescope (i.e. "on-axis"). If the fibre is moved at the location of the geometrical image on an object situated at the on-sky vector position β , the fibre mode M in the pupil plane becomes:

$$M_{\beta}(\mathbf{u}) = M(\mathbf{u}) e^{-ik\beta \cdot \mathbf{u}}, \quad (5)$$

and the coupled electric field becomes:

$$E = \iint_D A e^{i\Phi(\mathbf{u})} M(\mathbf{u}) e^{ik(\beta - \alpha) \cdot \mathbf{u}} d\mathbf{u}. \quad (6)$$

At this point, it is useful to note that since M is a positive non-zero function, we can define a scalar product $\langle \cdot | \cdot \rangle$ using:

$$\langle G | H \rangle = \iint_D G(\mathbf{u}) M(\mathbf{u}) H^*(\mathbf{u}) d\mathbf{u}, \quad (7)$$

as this expression has all the required properties (linearity, conjugate symmetry, and definite-positiveness). It is defined such that $\langle 1 | 1 \rangle = \sqrt{0.81}$ in the case where $M(\mathbf{u})$ is given as in Eq. (4).

Table 1. The eight electric fields inside the four fibres of a two-telescope dual-field interferometer.

Interferometer 1 (on-axis; $\beta = \mathbf{0}$)	Interferometer 2 (off-axis; $\beta = \alpha$)
$E_{\mathbb{A},1,\star} = A_{\star} \langle e^{i\Phi_{\mathbb{A}}(\mathbf{u})} 1 \rangle$	$E_{\mathbb{A},2,\star} = A_{\star} \langle e^{i\Phi_{\mathbb{A}}(\mathbf{u})} e^{-ik\alpha \cdot \mathbf{u}} \rangle$
$E_{\mathbb{A},1,\bullet} \approx 0$	$E_{\mathbb{A},2,\bullet} = A_{\bullet} \langle e^{i\Phi_{\mathbb{A}}(\mathbf{u})} 1 \rangle$
$E_{\mathbb{B},1,\star} = A_{\star} \langle e^{i\Phi_{\mathbb{B}}(\mathbf{u})} 1 \rangle$	$E_{\mathbb{B},2,\star} = A_{\star} \langle e^{i\Phi_{\mathbb{B}}(\mathbf{u})} e^{-ik\alpha \cdot \mathbf{u}} \rangle$
$E_{\mathbb{B},1,\bullet} \approx 0$	$E_{\mathbb{B},2,\bullet} = A_{\bullet} e^{-ik\alpha \cdot \mathbf{B}} \langle e^{i\Phi_{\mathbb{B}}(\mathbf{u})} 1 \rangle$

Notes. In this table $\Phi_{\mathbb{A}}(\mathbf{u})$ and $\Phi_{\mathbb{B}}(\mathbf{u})$ are the phase aberrations of, respectively, telescopes \mathbb{A} and \mathbb{B} .

With this notation, the electric field of Eq. (6) is simply the scalar product of the pupil-plane electric field and a complex exponential representing the offset between the source and the fibre:

$$E = A \langle e^{i\Phi(\mathbf{u})} | e^{ik(\alpha-\beta) \cdot \mathbf{u}} \rangle. \quad (8)$$

This formulation simplifies the expression of the fields injected into the fibres of the dual-field interferometer. These fields are summarized in Table 1 for the telescopes \mathbb{A} and \mathbb{B} . The first set of fields considers a star radiating with a flux $F_{\star} = A_{\star}^2$ located on the optical axis. The second set involves a planet with a flux $F_{\bullet} = A_{\bullet}^2$ positioned at α . For the first interferometer, we assume $\beta = \mathbf{0}$. For the second interferometer, we assume $\beta = \alpha$.

The two quantities of interest which are derived from the observations on the two interferometers are the coherent energies, denoted Γ , and given by:

$$\Gamma_1 = E_{\mathbb{A},1,\star} E_{\mathbb{B},1,\star}^* \quad (9)$$

$$\Gamma_2 = E_{\mathbb{A},2,\star} E_{\mathbb{B},2,\star}^* + E_{\mathbb{A},2,\bullet} E_{\mathbb{B},2,\bullet}^* \quad (10)$$

where we implicitly neglect the exoplanet light in the first interferometer. The exoplanet signal $\Gamma_{2,\bullet} = E_{\mathbb{A},2,\bullet} E_{\mathbb{B},2,\bullet}^*$ is observable in the second interferometer, blended with some amount of residual stellar coherent energy $\Gamma_{2,\star} = E_{\mathbb{A},2,\star} E_{\mathbb{B},2,\star}^*$. In the rest of the paper, we usually refer to $\Gamma_{2,\star}$ as "coherent speckle", by analogy with the speckles observed by classical imaging.

In practice, though, the coherent energies Γ are never observed directly, but are rather derived from measurements of the interference patterns as a function of optical delay x , described by:

$$I_1(x) = |E_{\mathbb{A},1,\star}|^2 + |E_{\mathbb{B},1,\star}|^2 + 2\Re[\Gamma_1 e^{ix}], \quad (11)$$

$$I_2(x) = |E_{\mathbb{A},2,\star}|^2 + |E_{\mathbb{B},2,\star}|^2 + |E_{\mathbb{A},2,\bullet}|^2 + |E_{\mathbb{B},2,\bullet}|^2 + 2\Re[\Gamma_2 e^{ix}]. \quad (12)$$

A common beam combination pattern is the ABCD scheme, for which the detectors of the interferometers record $I_1(x)$ and $I_2(x)$ as a function of four well-calibrated values of x : $0, \pi/2, \pi, 3\pi/2$. The coherent energies Γ_1 and Γ_2 are then reconstructed by a proper linear combination of these measurements.

2.3. Signal to Noise

In the numerator of the S/N, the signal can have multiple definitions:

$$S_{\text{entrance}} = \gamma F_{\bullet} \quad (13)$$

$$S_{\text{interfero}} = \gamma \Gamma_{2,\bullet} = \gamma F_{\bullet} \eta_{\bullet}^{\text{inj}} \quad (14)$$

$$S_{\text{processed}} = \gamma \Gamma_{2,\bullet} \eta_{\bullet}^{\text{proc}} = \gamma F_{\bullet} \eta_{\bullet}^{\text{inj}} \eta_{\bullet}^{\text{proc}}. \quad (15)$$

The definition of S_{entrance} in Eq. (13) corresponds to the number of photons of exoplanetary origin entering the interferometer. It depends solely on the flux of the exoplanet $F_{\bullet} = A_{\bullet}^2$ with a proportionality factor γ that encompasses the observation parameters. S_{entrance} represents an upper limit of the signal that we can expect.

The definition of $S_{\text{interfero}}$ used in Eq. (14) corresponds to the number of coherent exoplanetary photons that we can observe. To simplify the study, we assume a visibility of one, meaning that the exoplanet flux is fully coherent. Compared to S_{entrance} , $S_{\text{interfero}}$ is therefore reduced by the injection losses of the light into the single-mode fibre. These losses are denoted as $\eta_{\bullet}^{\text{inj}}$ and correspond to the product of two scalar products as in Eq. (8) averaged over time. Its value is always below 1 and is formally discussed in Section 2.5.

The definition of $S_{\text{processed}}$ in Eq. (15) includes an additional term, $\eta_{\bullet}^{\text{proc}}$, accounting for the post-processing of the data that reduces the amount of detectable signal ($\eta_{\bullet}^{\text{proc}} < 1$). This term depends on the algorithm used for post-processing and is described in Section 2.6.

The term γ is a proportionality factor that converts the flux into the signal in units of photons. This conversion factor incorporates several terms: the total observation duration (Δt), the telescope's collecting area ($\pi D^2/4$), the spectral bandwidth ($\Delta\lambda/\lambda$), the transmission efficiency (T_r), and Planck's constant (h):

$$\gamma = \rho \times \frac{1}{h} \times \frac{\Delta\lambda}{\lambda} \times \frac{\pi D^2}{4} \times T_r \times \Delta t. \quad (16)$$

The coefficient ρ corresponds to how the flux of a telescope is dispatched between the different interferometric baselines. Under the assumption that all baselines are recombined, it is equal to the number of telescopes divided by the maximum number of baselines:

$$\rho = N_{\text{tel}} \times \left(\frac{N_{\text{tel}}(N_{\text{tel}} - 1)}{2} \right)^{-1} = \frac{2N_{\text{tel}}}{N_{\text{tel}}^2 - N_{\text{tel}}}. \quad (17)$$

Thus, we have $\rho = 2$ for a two-telescope interferometer and $\rho = 2/3$ for the recombination of the 4 UTs with the GRAVITY instrument. The signal is then defined for a specific baseline, while the signals from multiple baselines can be combined to obtain the final S/N in Section 3.

In the denominator of the S/N, the noise can be broken into its individual and independent components:

$$N = \sqrt{N_{\text{readout}}^2 + N_{\text{thermal}}^2 + N_{\text{shot}}^2 + N_{\text{speckle}}^2}, \quad (18)$$

where the individual noise elements account for detector readout noise, thermal background photon noise, shot noise, and speckle noise. These elements are discussed in the following subsections.

Combining all sources of noise, and using $S_{\text{processed}}$ for the signal, the S/N ratio takes the form:

$$S/N = \frac{\gamma F_{\bullet} \eta_{\bullet}^{\text{inj}} \eta_{\bullet}^{\text{proc}}}{\sqrt{N_{\text{readout}}^2 + N_{\text{thermal}}^2 + N_{\text{shot}}^2 + N_{\text{speckle}}^2}}. \quad (19)$$

2.4. Readout and thermal background noise

The detector readout noise, N_{readout} , depends on the characteristics of the detector, on the number of frames and on the number

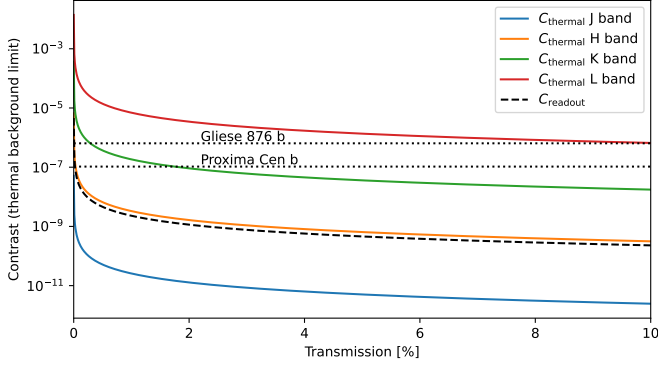


Fig. 2. Contrast limit at the VLTI as a function of the total transmission of the interferometer. The coloured curves represent theoretical contrast limits set by the thermal background of the telescope and interferometric laboratory (300 K). The dashed curves indicate the contrast limit from detector readout noise. The simulation parameters are detailed in Table 2.

of used pixels:

$$N_{\text{readout}} = \sigma_{e^-} \sqrt{4 \times \frac{3\Delta\lambda}{\delta\lambda} \times \frac{\Delta t}{\delta t}} \quad (20)$$

where σ_{e^-} represents the read noise per pixel per frame. For modern Teledyne H2RG detectors using a Fowler-16 detection readout scheme, σ_{e^-} is typically around 5 electrons. The term under the square root quantifies the total number of reads during the entire observation. The factor of 4 accounts for the ABCD recombination scheme. The spectral bandwidth is expressed as $\Delta\lambda$ and the spectral resolution is denoted by $\delta\lambda$. With an oversampling factor of 3, the total number of pixels across the band is $3\Delta\lambda/\delta\lambda$. The number of frames is given by the ratio of the total integration time to the detector integration time, $\Delta t/\delta t$.

The thermal background noise, N_{thermal} , can be estimated by assuming that blackbody emission from the laboratory at temperature T_{lab} is the dominant source of background. This assumption is reasonable given the low throughput ($T_r < 10\%$) of the optical chain, i.e. sky background can be neglected. The background emission is analytically estimated using the limited acceptance angle of a single-mode fibre:

$$N_{\text{thermal}} = \rho \times \sqrt{(1 - T_r) \times \frac{2c \Delta\lambda \Delta t}{\lambda^2 (\exp(\frac{hc}{kT_{\text{lab}}\lambda}) - 1)}}, \quad (21)$$

which can be simplified by using the Planck's law for a blackbody radiation $B_\lambda(T_{\text{lab}}, \lambda)$:

$$N_{\text{thermal}} = \sqrt{\gamma \times \frac{4}{\pi D^2 T_r} \times (1 - T_r) \times \lambda^2 \times B_\lambda(T_{\text{lab}}, \lambda)}. \quad (22)$$

The term λ^2 represents the étendue of the single-mode fibre. The factor γ is expressed by Eq. (16) and denotes the conversion factor between an incoming flux and the number of detected photons in our instrumental system.

To better understand the contrasts accessible with these readout and thermal background noise sources, we can convert these noise expressions into first-order contrast limits, by writing the planet raw signal as a function of the stellar flux:

$$S_{\text{entrance}} = \gamma C F_\star, \quad (23)$$

where C is the planet to star contrast ratio: $C = F_\bullet/F_\star$.

Table 2. Simulation parameters

	Fig. 2	Fig. 4	Fig. 5	Fig. 6
F_\star	10 Jy	10 Jy		10 Jy
δt	100 s	100 s		100 s
Δt	3 h	3 h		3 h
T_r	0-10%	5%		5%
T_{lab}	300 K	300 K		300 K
D	8	8	8	8
N_{tel}	2	2	2	2
$\Delta\lambda/\lambda$	0.23	0.23	0.23	0.23
$\lambda/\delta\lambda$	100	100	100	100
λ_B	J/H/K/L	I/K	K	I/J/H/K/L
Strehl		98	98	88/98
$ B $			100/200 m	100/200 m
n_{poly}			3-7-11	11

Notes. F_\star is flux of the stellar host. δt is the integration time of individual frames while Δt the total integration time. T_r is the total transmission of the instrument, D is the diameter of the telescopes and N_{tel} is the number of telescopes. $\Delta\lambda/\lambda$ the spectral bandwidth and $\lambda/\delta\lambda$ is the spectral resolution. λ_B is the name of the spectral band. $|B|$ is the projected baseline length, while n_{poly} is the polynomial order used for stellar light post processing.

Using a threshold of S/N = 3, this gives two contrast limits set respectively by the amount of readout and thermal background noise:

$$C_{\text{readout}} = 3 \frac{\sigma_{e^-}}{\gamma F_\star} \sqrt{4 \frac{3\Delta\lambda}{\delta\lambda} \frac{\Delta t}{\delta t}}, \quad (24)$$

$$C_{\text{thermal}} = 3 \frac{1}{\sqrt{\gamma} F_\star} \sqrt{\frac{4(1 - T_r)}{\pi D^2 T_r} \lambda^2 B_\lambda(300 \text{ K}, \lambda)}. \quad (25)$$

Both C_{readout} and C_{thermal} are depicted in Fig. 2 for a two telescopes interferometer with parameters as in Table 2. For comparison, Figure 2 also shows the contrast ratios in reflected light expected for two known planets: Gliese 876 b and Proxima Centauri b. This plot demonstrates the importance of high transmission, especially given the inherent low brightness of exoplanets. At a transmission of 2%, typical of the VLTI, the readout noise begins to limit detection slightly above 10^{-9} . The thermal emission equals readout noise near the H band. At longer wavelengths, near 3 microns, the 300 K emission of the laboratory strongly limits the achievable contrast and impedes the observation of reflected light from Gliese 876 b and Proxima Centauri b.

2.5. Starlight Suppression

2.5.1. Attenuation Formulas

At short wavelengths, thermal background noise and readout noise limit the achievable contrast to values of $\sim 10^{-9}$. Unfortunately, the shot noise caused by stellar speckles can be several orders of magnitude above this limit. Therefore, it is necessary to remove as much of this parasitic light as possible, a process known as starlight suppression.

For high-contrast interferometry, we propose leveraging the efficient spatial filtering provided by single-mode fibres. This filtering can be combined with pupil-plane phase apodization, which can achieve near-perfect rejection of stellar light into the fibre. The effect of the apodization can be modeled with two coupling coefficients: one affecting the stellar light (η_\star^{inj}) and the

other the planetary light ($\eta_{\bullet}^{\text{inj}}$). The shot noise caused by the stellar flux then becomes:

$$N_{\text{shot}} = \sqrt{\gamma F_{\star} \eta_{\star}^{\text{inj}}}, \quad (26)$$

while the exoplanet signal is given by:

$$S_{\text{interfero}} = \gamma F_{\bullet} \eta_{\bullet}^{\text{inj}}. \quad (27)$$

Phase apodization works by adding an extra phase term $\Psi(\mathbf{u})$ in the pupil-plane of the telescope, for example using an offset to the deformable mirror of the AO. With this additional phase term in the pupil-plane, the coupling formulas for the electric field in the second interferometer (see Table 1) are given by:

$$E_{2,\star} = A_{\star} \langle e^{i\Phi(\mathbf{u})+i\Psi(\mathbf{u})} | e^{-i\mathbf{k}\alpha\cdot\mathbf{u}} \rangle \quad (28)$$

$$E_{2,\bullet} = A_{\bullet} \langle e^{i\Phi(\mathbf{u})+i\Psi(\mathbf{u})} | 1 \rangle \quad (29)$$

and the corresponding apodization coefficients are:

$$\eta_{\star}^{\text{inj}} = \frac{|E_{2,\star}|^2}{F_{\star}} = |\langle e^{i\Phi(\mathbf{u})+i\Psi(\mathbf{u})} | e^{-i\mathbf{k}\alpha\cdot\mathbf{u}} \rangle|^2 \quad (30)$$

$$\eta_{\bullet}^{\text{inj}} = \frac{|E_{2,\bullet}|^2}{F_{\bullet}} = |\langle e^{i\Phi(\mathbf{u})+i\Psi(\mathbf{u})} | 1 \rangle|^2. \quad (31)$$

These expressions are valid for a single value of the wavevector k . For a polychromatic source, these expressions must be integrated over the waveband to obtain appropriate values for the apodization coefficients.

2.5.2. Designing a Phase Apodizer

The overall objective of a good apodization scheme is of course to minimize the value of $\eta_{\star}^{\text{inj}}$ while maximizing the value of $\eta_{\bullet}^{\text{inj}}$. There are various strategies for doing so, as multiple solutions exist. State-of-the-art techniques, which include the solutions proposed by Por (2020) or Haffert et al. (2020), leverage from an iterative optimization algorithm (Por 2017).

In this study, we adopt a more qualitative approach, which takes advantage of the fact that we are only interested in minimizing the flux at a particular position, corresponding to the location of the fibre. Therefore, we know in advance for which value of α our apodization function Ψ_{α} should be designed. We use a two-step process: the first step involves a slight simplification of the apodization problem to derive a simple analytical solution, which is then used as a starting point for a numerical optimization to derive the final apodization function. This second step is ultimately intended to be performed in real-time using a dedicated control-loop in the instrument, the details of which are outside the scope of the present study.

To derive an analytical solution, we first simplify the problem by ignoring the impact of atmospheric fluctuations, setting $\Phi(\mathbf{u}) = 0$ in Eq. (30) and (31). We also simplify the apodization function by enforcing a set of symmetries. Specifically, we look for a solution that is a function of $\alpha \cdot \mathbf{u}$ (axially symmetric) and anti-centrosymmetric¹:

$$\Psi_{\alpha}(\mathbf{u}) = \Psi_{\alpha}(\mathbf{u}') \quad \text{if} \quad \alpha \cdot \mathbf{u} = \alpha \cdot \mathbf{u}', \quad (32)$$

$$\Psi_{\alpha}(\mathbf{u}) = -\Psi_{\alpha}(-\mathbf{u}). \quad (33)$$

¹ A similar derivation can also be done without the anti-centrosymmetry requirement, in the case where we want to cancel imaginary speckles

We also assume that the apodization function is small, i.e. that $\Psi_{\alpha}(\mathbf{u}) \ll 1$. This is consistent with the requirement that $\eta_{\bullet}^{\text{inj}}$ should be as close to 1 as possible. This can be seen by using a linear development of Eq. (31) to the second order:

$$\eta_{\bullet}^{\text{inj}} = |\langle e^{i\Psi_{\alpha}(\mathbf{u})} | 1 \rangle|^2 \simeq \left| \langle 1 | 1 \rangle - \frac{1}{2} \langle \Psi_{\alpha}(\mathbf{u}) | \Psi_{\alpha}(\mathbf{u}) \rangle \right|^2. \quad (34)$$

The first order has canceled out due to the central symmetry of Ψ_{α} : $\langle \Psi_{\alpha} | 1 \rangle = 0$. Also, we made use the fact that Ψ is a real function, which implies $\langle \Psi_{\alpha}^2 | 1 \rangle = \langle \Psi_{\alpha} | \Psi_{\alpha} \rangle$ from the definition of $\langle \cdot | \cdot \rangle$ given in Eq. (7). With such a form, $\eta_{\bullet}^{\text{inj}}$ can be expected to be close to $\langle 1 | 1 \rangle = 0.81$ if Ψ_{α} is small.

The first order development of Eq. (30) for the starlight apodization, however, gives:

$$\eta_{\star}^{\text{inj}} = |\langle e^{i\Psi_{\alpha}(\mathbf{u})} | e^{-i\mathbf{k}\alpha\cdot\mathbf{u}} \rangle|^2 \quad (35)$$

$$\simeq \left| \langle 1 | e^{-i\mathbf{k}\alpha\cdot\mathbf{u}} \rangle + \langle i\Psi_{\alpha}(\mathbf{u}) | e^{-i\mathbf{k}\alpha\cdot\mathbf{u}} \rangle \right|^2 \quad (36)$$

$$\simeq \left| \langle 1 | \cos(\mathbf{k}\alpha \cdot \mathbf{u}) \rangle - \langle \Psi_{\alpha}(\mathbf{u}) | \sin(\mathbf{k}\alpha \cdot \mathbf{u}) \rangle \right|^2, \quad (37)$$

where the last line makes use of the fact that $\langle 1 | \sin(\mathbf{k}\alpha \cdot \mathbf{u}) \rangle$ and $\langle \Psi_{\alpha}(\mathbf{u}) | \cos(\mathbf{k}\alpha \cdot \mathbf{u}) \rangle = 0$ due to the definition of $\langle \cdot | \cdot \rangle$ and the symmetries of the functions involved. This equation shows that the injected starlight can be minimized by setting:

$$\langle \Psi_{\alpha}(\mathbf{u}) | \sin(\mathbf{k}\alpha \cdot \mathbf{u}) \rangle = \langle 1 | \cos(\mathbf{k}\alpha \cdot \mathbf{u}) \rangle. \quad (38)$$

This guarantees that the injected starlight is 0 at the particular wavevector k , but does not guarantee that the injected light is minimum over the entire waveband. If the waveband is small enough, minimization over the entire band can be ensured by setting the successive derivatives of $\eta_{\star}^{\text{inj}}$ with respect to k to 0. The first and second derivatives are given by:

$$\frac{d\eta_{\star}^{\text{inj}}}{dk} = 2\langle e^{i\Psi_{\alpha}(\mathbf{u})} | e^{-i\mathbf{k}\alpha\cdot\mathbf{u}} \rangle \Re\left(\langle e^{i\Psi_{\alpha}(\mathbf{u})} | [-i\alpha \cdot \mathbf{u}] e^{-i\mathbf{k}\alpha\cdot\mathbf{u}} \rangle\right), \quad (39)$$

$$\begin{aligned} \frac{d^2\eta_{\star}^{\text{inj}}}{dk^2} &= 2\langle e^{i\Psi_{\alpha}(\mathbf{u})} | [-i\alpha \cdot \mathbf{u}] e^{-i\mathbf{k}\alpha\cdot\mathbf{u}} \rangle \Re\left(\langle e^{i\Psi_{\alpha}(\mathbf{u})} | [-i\alpha \cdot \mathbf{u}] e^{-i\mathbf{k}\alpha\cdot\mathbf{u}} \rangle\right) \\ &\quad + 2\langle e^{i\Psi_{\alpha}(\mathbf{u})} | e^{-i\mathbf{k}\alpha\cdot\mathbf{u}} \rangle \frac{d\Re\left(\langle e^{i\Psi_{\alpha}(\mathbf{u})} | [-i\alpha \cdot \mathbf{u}] e^{-i\mathbf{k}\alpha\cdot\mathbf{u}} \rangle\right)}{dk}. \end{aligned} \quad (40)$$

Given our previous Eq. (38), which guarantees that $\eta_{\star}^{\text{inj}} = |\langle e^{i\Psi_{\alpha}(\mathbf{u})} | e^{-i\mathbf{k}\alpha\cdot\mathbf{u}} \rangle|^2 = 0$, the first derivative is necessary 0, and the second derivative can be simplified to:

$$\frac{d^2\eta_{\star}^{\text{inj}}}{dk^2} = 2\langle e^{i\Psi_{\alpha}(\mathbf{u})} | [i\alpha \cdot \mathbf{u}] e^{-i\mathbf{k}\alpha\cdot\mathbf{u}} \rangle \Re\left(\langle e^{i\Psi_{\alpha}(\mathbf{u})} | [i\alpha \cdot \mathbf{u}] e^{-i\mathbf{k}\alpha\cdot\mathbf{u}} \rangle\right). \quad (41)$$

This last expression shows that canceling the second derivative of $\eta_{\star}^{\text{inj}}$ with respect to k requires canceling out the real part of $\langle e^{i\Psi_{\alpha}(\mathbf{u})} | [i\mathbf{k}\alpha \cdot \mathbf{u}] e^{-i\mathbf{k}\alpha\cdot\mathbf{u}} \rangle$, where we took advantage of the linearity of the scalar product to add a factor k in the second term and keep all elements dimensionless.

By using again the first-order development of $e^{i\Psi_{\alpha}}$ and the different symmetries, we find:

$$\begin{aligned} \Re\left(\langle e^{i\Psi_{\alpha}(\mathbf{u})} | [i\mathbf{k}\alpha \cdot \mathbf{u}] e^{-i\mathbf{k}\alpha\cdot\mathbf{u}} \rangle\right) &\simeq \langle 1 | [\mathbf{k}\alpha \cdot \mathbf{u}] \sin(\mathbf{k}\alpha \cdot \mathbf{u}) \rangle \\ &\quad + \langle \Psi_{\alpha}(\mathbf{u}) | [\mathbf{k}\alpha \cdot \mathbf{u}] \cos(\mathbf{k}\alpha \cdot \mathbf{u}) \rangle, \end{aligned} \quad (42)$$

which shows that in order to cancel out this real part, we need:

$$\langle \Psi_{\alpha}(\mathbf{u}) | [\mathbf{k}\alpha \cdot \mathbf{u}] \cos(\mathbf{k}\alpha \cdot \mathbf{u}) \rangle = -\langle 1 | [\mathbf{k}\alpha \cdot \mathbf{u}] \sin(\mathbf{k}\alpha \cdot \mathbf{u}) \rangle. \quad (43)$$

Putting everything together, to solve our apodization problem, we are therefore looking for a function Ψ_α such that:

$$\langle \Psi_\alpha(\mathbf{u}) | \Psi_\alpha(\mathbf{u}) \rangle = \|\Psi_\alpha\|^2 \text{ is as small as possible,} \quad (44)$$

$$\langle \Psi_\alpha(\mathbf{u}) | H_1(\mathbf{u}) \rangle = z_1, \quad (45)$$

$$\langle \Psi_\alpha(\mathbf{u}) | H_2(\mathbf{u}) \rangle = z_2, \quad (46)$$

where:

$$H_1(\mathbf{u}) = \sin(k\alpha \cdot \mathbf{u}), \quad (47)$$

$$z_1 = \langle 1 | \cos(k\alpha \cdot \mathbf{u}) \rangle, \quad (48)$$

$$H_2(\mathbf{u}) = [k\alpha \cdot \mathbf{u}] \cos(k\alpha \cdot \mathbf{u}), \quad (49)$$

$$z_2 = -\langle 1 | [k\alpha \cdot \mathbf{u}] \sin(k\alpha \cdot \mathbf{u}) \rangle. \quad (50)$$

This system is readily solved by noting that in order to minimize its norm in Eq. (44), while fulfilling the two conditions given by Eq. (45) and (46), Ψ_α needs to be in the plane defined by (H_1, H_2) :

$$\Psi_\alpha = aH_1 + bH_2. \quad (51)$$

Then, solving the linear system resulting from Eq. (45) and (46) gives the following closed-form solution for Ψ_α :

$$\Psi_\alpha = \frac{z_1 \|H_2\|^2 - z_2 \langle H_1 | H_2 \rangle}{\|H_1\|^2 \|H_2\|^2 - \langle H_1 | H_2 \rangle^2} H_1 + \frac{z_2 \|H_1\|^2 - z_1 \langle H_1 | H_2 \rangle}{\|H_1\|^2 \|H_2\|^2 - \langle H_1 | H_2 \rangle^2} H_2. \quad (52)$$

This closed-form solution for the apodization is valid under the conditions that Ψ_α remains small and in the absence of atmospheric fluctuations. It also ignores the true dependency of the injected flux as a function of the wavelength, as we have only tried to cancel the flux at a particular wavenumber in Eqs. (45) and (46). Moreover, in practice, the optical path delays is applied by a deformable mirror and it is therefore in units of length. So our strategy is to use the solution given in Eq. (52) as an initial guess in an optimization process.

To do so, we keep Ψ_α as a linear combination of two functions H_1 and H_2 defined for a central wavenumber k_0 , and we directly integrate the square root of the scalar product over all wavenumbers k :

$$\eta_\star^{\text{inj}}(a, b) = \int_{k_0 - \Delta k/2}^{k_0 + \Delta k/2} \left| \langle e^{i \frac{k}{k_0} [a \sin(k_0 \alpha \cdot \mathbf{u}) + b k_0 \alpha \cdot \mathbf{u} \cos(k_0 \alpha \cdot \mathbf{u})]} | e^{-ik\alpha \cdot \mathbf{u}} \rangle \right|^2 \frac{dk}{\Delta k}. \quad (53)$$

This apodization coefficient can then be numerically minimized to find the coefficients a and b :

$$(a, b) = \text{argmin} \left\{ \eta_\star^{\text{inj}}(a, b) \right\}, \quad (54)$$

which will give a set of values (a, b) for any value of the angular separation α .

In Figure 3, we show the values of the coefficients a and b obtained both by the closed-form solution of the approximated apodization problem from Eq. (52), and after the optimization process from Eq. (54), as a function of the separation α . Also shown are the apodization functions $aH_1 + bH_2$ for the two specific cases of $\alpha = \lambda/D$ and $\alpha = 2\lambda/D$.

2.5.3. Photon noise after pupil apodization

To calculate the amount of photon noise introduced by the starlight, we have to account for the atmospheric perturbations. To do so, we simulated the atmospheric perturbations using

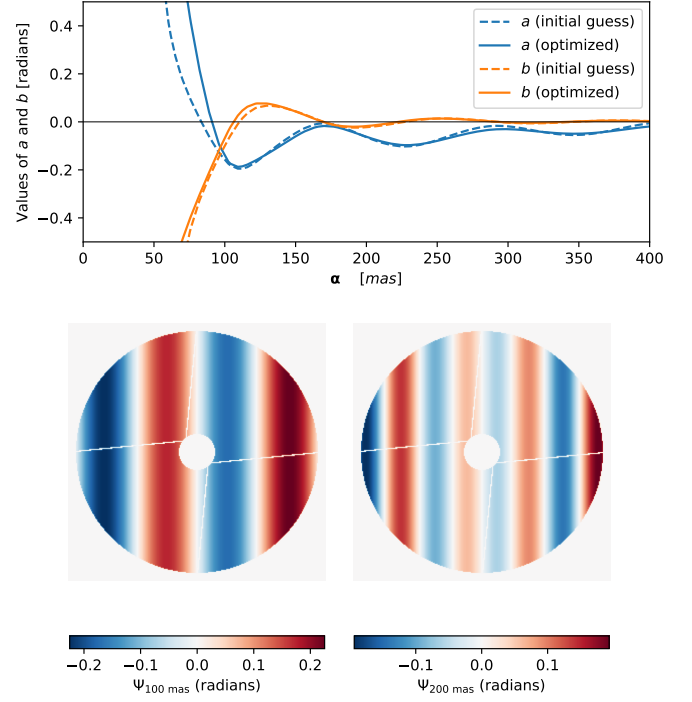


Fig. 3. Upper panel: Coefficients (a, b) used to compute the phase apodizer as $\Psi_\alpha = aH_1 + bH_2$. The solid lines show the optimized coefficient used in the final definition of the apodizer, i.e. the solution of Eq. (54). The dashed lines show the initial guess calculated from Eq. (52). The simulation has been made for K band observations ($k_0 = 2\pi/2.2 \mu\text{m}$) and the shape of the VLT pupil. Lower panels: The apodizer function, $\Psi_\alpha(\mathbf{u})$, for a target at an angular separation of 100 mas (left panel) and 200 mas (right panel).

HCIPy, a Python framework for high-contrast imaging simulation (Por et al. 2018). The atmospheric residuals are obtained using a closed-loop adaptive optics system similar to the one used in the SPHERE instrument, which employs a Shack-Hartmann Wavefront Sensor (WFS). The simulations include WFS Photon Noise and the Time Lag of the AO system. The aberrations have been adjusted to the lab measurements of the SAXO optimal performance, giving 98% in K band, and 72% in I band (Fusco et al. 2016).

The phase masks $\Phi(\mathbf{u})$ generated by the atmospheric residuals are then added to the phase mask $\Psi(\mathbf{u})$ of the apodizer to calculate the two broad band attenuations coefficients:

$$\eta_\star^{\text{inj}} = \int_{k_0 - \Delta k/2}^{k_0 + \Delta k/2} \left| \langle e^{i\Phi(\mathbf{u}) + i\Psi(\mathbf{u})} | e^{-ik\alpha \cdot \mathbf{u}} \rangle \right|^2 \frac{dk}{\Delta k} \quad (55)$$

and

$$\eta_\bullet^{\text{inj}} = \int_{k_0 - \Delta k/2}^{k_0 + \Delta k/2} \left| \langle e^{i\Phi(\mathbf{u}) + i\Psi(\mathbf{u})} | 1 \rangle \right|^2 \frac{dk}{\Delta k}. \quad (56)$$

The two panels of Figure 4 display simulations under these atmospheric conditions in the two bands. For reference, the dotted curves in both panels represent a system without atmosphere (Strehl ratio of 100%). These simulations use parameters representative of the VLTI, as listed in Table 2.

Figure 4 also shows the contrast limit obtained assuming a threshold of 3 on the S/N, using $S_{\text{interfero}}$ for the signal as defined in Eq. (27), and N_{shot} for the noise as defined by Eq. (26).

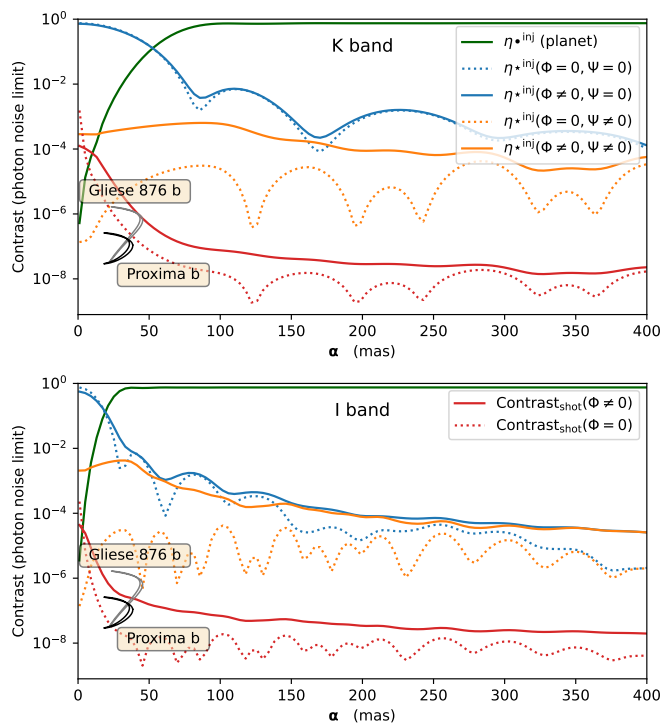


Fig. 4. Apodization due to the spatial filtering caused by single-mode fibres as a function of the angular separation α between the star and the exoplanet, in the K band (upper panel) and in the I band (lower panel). The green curves show $\eta_{\star}^{\text{inj}}$, the injection of the exoplanet flux into interferometer 2, while the blue and orange curves represent the injection of the stellar flux ($\eta_{\star}^{\text{inj}}$). The blue curves are without a phase apodization ($\Psi_{\alpha} = 0$), while the orange curves are with phase apodization ($\Psi_{\alpha} = aH_1 + bH_2$). The solid curves include the residuals of atmospheric correction by an extreme AO system, giving a Strehl ratio of 98% in the K band and 72% in the I band. The dotted curves are obtained assuming no atmospheric residuals: $\Phi(\mathbf{u}) = 0$, hence a Strehl ratio of 100%. The red curves correspond to the contrast limit, C_{shot} in Eq (57), that would be achieved when limited by photon noise, for an observation with parameters as stipulated in Table 2. The phase apodizer is extremely efficient at decreasing the flux injected into the fibre in the K band. However, at shorter wavelengths, the lower Strehl ratio makes it less effective, with the injected flux mostly due to the atmospheric halo.

According to this threshold, the contrast is defined as follows:

$$C_{\text{shot}} = 3 \frac{1}{\sqrt{\gamma F_{\star}}} \frac{\sqrt{\eta_{\star}^{\text{inj}}}}{\eta_{\bullet}^{\text{inj}}}. \quad (57)$$

These curves indicate that the photon noise contrast limit is just sufficient to detect the exoplanet Gliese 876b in the K band. Proxima Cen b, on the other hand, is only observable at smaller angular separations and can only be detected at shorter wavelengths.

Achieving a high stellar extinction $1/\eta_{\star}^{\text{inj}}$ of at least 10^3 is crucial for observing exoplanets with contrast ratios around 10^{-8} . This can potentially be achieved at long wavelengths with very high Strehl and excellent apodization, or by taking advantage of the smaller diffraction spot at short wavelengths, which somewhat loosens the requirements on the Strehl ratio and apodization.

2.6. Coherent Speckle Removal

2.6.1. Principle of post-processing

Due to the chromatic behaviour of stellar light and due to residual optical aberrations, an apodizer alone cannot completely eliminate the coherent stellar light. However, the residual coherent speckles can be removed by a dedicated post-processing algorithm. This is similar to what happens in direct-imaging, where the use of a coronagraph is always complemented by a post-processing technique (for example ADI or SDI) to reach the highest levels of contrast.

In dual-field interferometry, the residual coherent speckles can be removed by taking advantage of the simultaneous observation of the central-star by the first interferometer. A coherent flux $\Gamma_{1,\star}$ is measured on the first interferometer (see Figure 1), which can be used to phase-reference the stellar coherent speckles on the second interferometer, thanks to the internal monitoring of the non-common optical path by the metrology.

In practice, the two coherent fluxes $\Gamma_{1,\star}$ and $\Gamma_{2,\star}$ are not equal, as they can have vastly different amplitudes. But they remain similar in the sense that neither their phase, nor their spectral shape are significantly different. Experience shows that these differences are well captured by a low-order polynomial in k , the wavenumber:

$$\frac{\Gamma_{2,\star}}{\Gamma_{1,\star}} = \sum_{n=0}^{n_{\text{poly}}} a_n k^n, \quad (58)$$

where the coefficients a_n are complex-coefficients which represent the chromatic difference between the on-axis stellar light $\Gamma_{1,\star}$ and the off-axis stellar light $\Gamma_{2,\star}$. The order n_{poly} is typically 5 to 15 for a good approximation².

Another advantage of using a metrology system to reference one interferometer to the other is the ability to phase reference the planet light as well. It guarantees that the phase of the coherent flux observed in the second interferometer will follow the analytical formula for a binary companion at a given separation α :

$$\frac{\Gamma_{2,\bullet}}{\Gamma_{1,\star}} = \left(\frac{F_{\bullet}}{F_{\star}} \right) e^{-ik(\alpha \cdot B)} = C e^{-ik(\alpha \cdot B)}, \quad (59)$$

ignoring the spectral differences between the planet and the star by reducing the contrast F_{\bullet}/F_{\star} to a single parameter C .

Hence, there is a structural difference between the phase of the low-order polynomial-like off-axis coherent flux, $\arg(\Gamma_{2,\star})$, and the phase of planet coherent flux, $\arg(\Gamma_{2,\bullet})$. It is this difference which is used to filter out $\Gamma_{2,\star}$ from the combined coherent signal $\Gamma_2 = \Gamma_{2,\star} + \Gamma_{2,\bullet}$ without significantly impacting the second. This idea is at the heart of the ExoGRAVITY Collaboration's post-processing technique, pioneered in GRAVITY Collaboration et al. (2019) and detailed in GRAVITY Collaboration et al. (2020a). In the rest of this Section, we use the algorithms detailed in these publications to estimate the residual stellar contamination N_{speckle} in Eq. (19).

2.6.2. Mathematical formulation

As outlined by GRAVITY Collaboration et al. (2020a) and Nowak et al. (2020), the formalism of the ExoGRAVITY method involves considering all wavelength-dependant quantities as

² We also tested spline-based linear models, similar to those used by Ruffio et al. (2019, 2023) to model the continuum, but did not observe any improvement for an identical number of degrees of freedom.

column-vectors. In this formalism, the coherent flux Γ is a column-vector $[\Gamma(k_1), \Gamma(k_2), \dots, \Gamma(k_n)]^T$. Retrieving the value of C involves two steps: (1) projecting the coherent flux vector Γ_2 onto a subspace orthogonal to that of the coherent speckle model of $\Gamma_{2,\star}$; (2) projecting the theoretical planet coherent flux from Eq. (59) onto this same subspace to retrieve the contrast C .

In the first step, the subspace orthogonal to the coherent speckle is calculated from the series of vectors J_n and Q_n defined as:

$$J_n = k^n \Gamma_{1,\star} \quad (60)$$

$$Q_n = ik^n \Gamma_{1,\star}. \quad (61)$$

The projector P_\perp on the subspace orthogonal to all the J_n and Q_n , $n \in \{0, \dots, n_{\text{poly}}\}$ is the matrix P_\perp defined by:

$$P_\perp = I_{n_{\text{poly}}} - \sum_{n=0}^{n_{\text{poly}}} \left[\frac{J_n^T}{J_n^T \cdot J_n} + \frac{Q_n^T}{Q_n^T \cdot Q_n} \right]. \quad (62)$$

The first step therefore consists in multiplying the coherent flux by P_\perp :

$$P_\perp \cdot \Gamma_2 = P_\perp \cdot \Gamma_{2,\star} + P_\perp \cdot \Gamma_{2,\bullet}, \quad (63)$$

with the hope that the starlight residual, $P_\perp \cdot \Gamma_{2,\star}$, will be close to 0.

In the second step, we calculate the vector:

$$K_\alpha = P_\perp \cdot \left[\Gamma_{1,\star} e^{-ik(\alpha \cdot B)} \right], \quad (64)$$

which serves as a model for the coherent flux of the exoplanet $\Gamma_{2,\bullet}$, as expected according to Eqs. (59), projected in the same subspace as the data. Assuming $P_\perp \cdot \Gamma_{2,\star} = 0$, we now have:

$$P_\perp \cdot \Gamma_2 = CK_\alpha, \quad (65)$$

which gives the solution:

$$C = \frac{K_\alpha^T \cdot P_\perp}{K_\alpha^T \cdot K_\alpha} \cdot \Gamma_2. \quad (66)$$

This product post-processing is required to extract the planet signal from the stellar speckles, but it also attenuates the signal by reducing $\Gamma_{2,\bullet}$.

2.6.3. Simulation of Post-Processing Attenuations

To calculate the level of attenuation of the coherent star and exoplanetary light, we must account for atmospheric perturbations. We again used HCIPy to simulate the wavefront residuals on two telescopes, each equipped with a SPHERE-like AO system with similar performance. As in Section 2.5.3, we then added a phase apodizer to obtain two sets of phase masks $\Phi_A(\mathbf{u})$ for telescope A and $\Phi_B(\mathbf{u})$ for telescope B. Both Φ_A and Φ_B depend on k and time.

The total attenuation can be calculated from the electric field expressed in Table 1:

$$\eta_\bullet^{\text{inj}} \eta_\bullet^{\text{proc}} = \frac{K_\alpha^T \cdot P_\perp}{K_\alpha^T \cdot K_\alpha} \cdot \begin{bmatrix} \langle e^{i\Phi_A(\mathbf{u})} | 1 \rangle \langle e^{i\Phi_B(\mathbf{u})} | 1 \rangle^* e^{-ik_1 \alpha \cdot B} \\ \vdots \\ \langle e^{i\Phi_A(\mathbf{u})} | 1 \rangle \langle e^{i\Phi_B(\mathbf{u})} | 1 \rangle^* e^{-ik_{n_\alpha} \alpha \cdot B} \end{bmatrix}. \quad (67)$$

Similarly, the attenuation of the coherent stellar speckle can be written as:

$$\eta_\star^{\text{inj}} \eta_\star^{\text{proc}} = \frac{K_\alpha^T \cdot P_\perp}{K_\alpha^T \cdot K_\alpha} \cdot \begin{bmatrix} \langle e^{i\Phi_A(\mathbf{u})} | e^{-ik_1 \alpha \cdot \mathbf{u}} \rangle \langle e^{i\Phi_B(\mathbf{u})} | e^{-ik_1 \alpha \cdot \mathbf{u}} \rangle^* \\ \vdots \\ \langle e^{i\Phi_A(\mathbf{u})} | e^{-ik_{n_\alpha} \alpha \cdot \mathbf{u}} \rangle \langle e^{i\Phi_B(\mathbf{u})} | e^{-ik_{n_\alpha} \alpha \cdot \mathbf{u}} \rangle^* \end{bmatrix}. \quad (68)$$

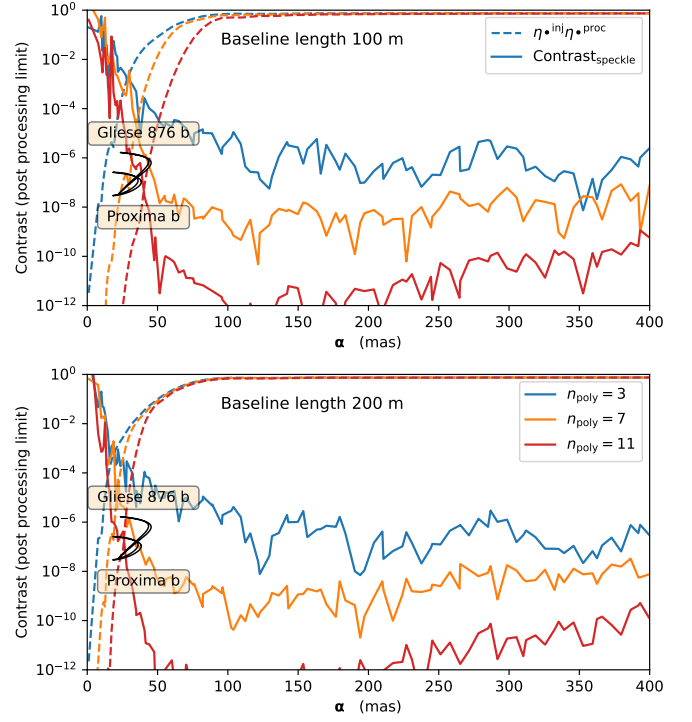


Fig. 5. Attenuation of the exoplanet signal ($\eta_\bullet^{\text{inj}} \eta_\bullet^{\text{proc}}$, in dashed lines) and the corresponding contrast limit ($C_{\text{speckle}} = 3\eta_\star^{\text{inj}} \eta_\star^{\text{proc}} / \eta_\bullet^{\text{inj}} \eta_\bullet^{\text{proc}}$, in solid lines) after post-processing of the stellar speckle, as a function of angular separation. The three colour curves represent three levels of polynomial fitting strength (n_{poly} of 3, 7, and 11) used for filtering the coherent speckles. The dotted curves show the attenuation of the exoplanet signal, illustrating that a lower polynomial order yield a smaller inner working angle. The solid curves indicate the contrast limit after post-processing of the stellar speckle, demonstrating that higher polynomial orders result in a better contrast limit. The upper plot represents observations with a 100 m baseline, while the lower plot corresponds to a 200 m interferometer baseline.

The attenuations due to apodization and post-processing are combined in our analysis because it is difficult to calculate the attenuation of post-processing without including the spatial filtering of the single-mode fibre.

This residual starlight, which is neither rejected by the fibre and the apodization nor by the post-processing algorithm, corresponds to the speckle noise term in Eq. (19):

$$N_{\text{speckle}} = \gamma F_\star \eta_\star^{\text{inj}} \eta_\star^{\text{proc}}. \quad (69)$$

In Figure 5, we show the evolution of $\eta_\bullet^{\text{inj}} \eta_\bullet^{\text{proc}}$ as a function of the angular separation α , for three different levels of aggressiveness in deconvolution, corresponding to three different orders for the polynomial model of the coherent residual starlight ($n_{\text{poly}} = 3, 7, \text{ and } 11$), and two baseline lengths: $B = 100$ m and 200 m. This graph shows how, as the planet gets closer to the central star ($\alpha \rightarrow 0$), its signal becomes too similar to the coherent flux of the central star and gets removed by the post-processing step ($\eta_\bullet^{\text{inj}} \eta_\bullet^{\text{proc}} \rightarrow 0$).

We also plot a contrast limit assuming a threshold of 3 on the S/N, using $S_{\text{processed}}$ for the signal as defined in Eq. (15), and N_{speckle} for the noise as defined in Eq. (69). According to this threshold, the contrast is defined as follows:

$$C_{\text{speckle}} = 3 \frac{\eta_\star^{\text{inj}} \eta_\star^{\text{proc}}}{\eta_\bullet^{\text{inj}} \eta_\bullet^{\text{proc}}}. \quad (70)$$

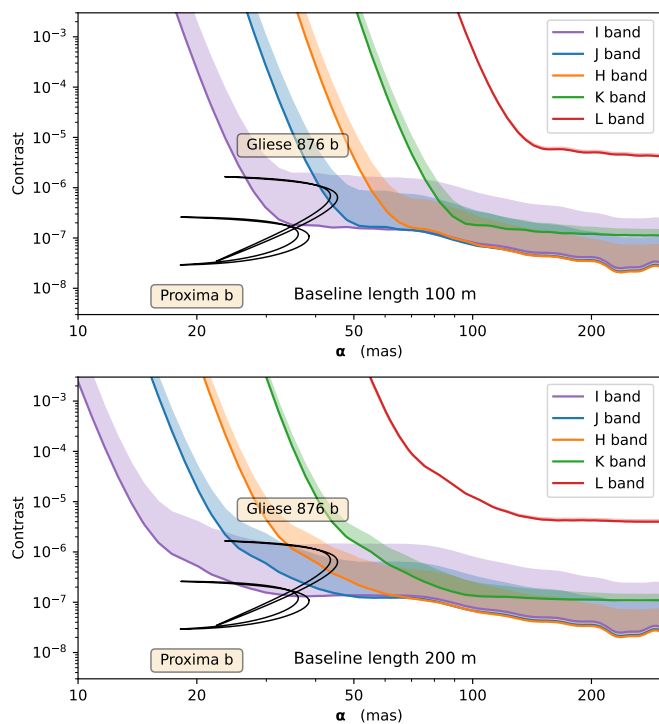


Fig. 6. Contrast limit as a function of angular separation, with simulation parameters detailed in Table 2. The upper panel illustrates the contrast dependence on waveband for a 100 m baseline. The lower panel displays the contrast limits for a 200 m baseline. The shaded area represents a range of K band Strehl ratios, from 88% (worse contrast limit) to 98% (best contrast limit). At short wavelength, the contrast range is limited by the Strehl. In the K and L bands, the contrast range is predominantly limited by thermal background noise. The inner working angles are constrained by both the telescope’s point spread function and the interferometric resolution, both linear function of wavelength.

2.7. Final Contrast Curve

Putting everything together, the contrast limit of a dual-field interferometer on the VLTI can be calculated using the formula presented in Eq. (19), replacing F_{\bullet} by $C F_{\star}$ to convert to contrast, and using an arbitrary threshold of $S/N = 3$ to define a detection limit:

$$C = 3 \frac{\sqrt{N_{\text{readout}}^2 + N_{\text{background}}^2 + \gamma F_{\star} \eta_{\star}^{\text{inj}} + (\gamma F_{\star} \eta_{\star}^{\text{inj}} \eta_{\star}^{\text{proc}})^2}}{\gamma F_{\star} \eta_{\bullet}^{\text{inj}} \eta_{\bullet}^{\text{proc}}}. \quad (71)$$

The resulting contrast curve is given in Figure 6.

This accounts for the cumulative effects of readout noise, thermal background noise, stellar photon noise, and residual speckle noise after post-processing, and provides critical insights into the system’s performance. As shown in the upper panel of Fig. 6, a contrast of 10^{-6} can be achieved at 25 mas in the I band, but this increases to 70 mas in the K band. Reducing the baseline length also results in an inversely proportional increase of the detection limit at low separations, highlighting the importance of baseline extension for reducing this angle beyond the current capabilities of the VLTI.

Another important observation relates to the Strehl ratio, which strongly influences the contrast that can be achieved, impacting both the signal injected into the fibre and the effectiveness of stellar flux apodization, as illustrated in Fig. 4. As anticipated, the Strehl ratio - and consequently, the contrast - is more

adversely affected at shorter wavelengths. Two distinct regimes are observed: in a regime of good correction, above a Strehl ratio of $\approx 50\%$ our simulations show a preference for shorter wavelengths due to the beneficial increase in angular resolution that compensates for the slight decrease in Strehl ratio. In the regime where the Strehl ratio is low, the correction quality is insufficient for proper light injection into the single-mode fibre, and the advantages of a narrower point spread function no longer offset the losses.

Furthermore, the figure underscores the difficulty of detecting reflected light from exoplanets beyond 2 microns, attributed to the escalation of thermal background noise. At these wavelengths, exploring thermal emissions from exoplanets emerges as a viable alternative, albeit likely requiring the colder operational conditions provided by space-based observatories.

3. An additional Unit Telescope in the context of exoplanet detection

3.1. The Effect of the 2D Geometry of the VLTI

Figure 6 shows how the contrast limit changes as a function of separation for baseline lengths of 100 and 200 m. However, this does not account for the geometry of the VLTI, which has six baselines. In practice, the geometry of the array is crucial, as the relevant quantity when determining the "baseline length" is the projected baseline vector, $\alpha \cdot \mathbf{B}/|\alpha|$, projected both in the plane of the sky and along the position angle of the exoplanet.

The projection along the plane of the sky depends on the position of the star. In the upper panel of Fig. 7, the UV coverage is shown for Proxima Cen when it passes the meridian, representing almost optimal conditions. The frequency domain covered by the VLTI (red points) is mostly constrained in the North-East direction due to the intrinsically elongated geometry of the VLTI along the UT1-UT4 baseline.

The second projection is along the position angle (PA) of the exoplanet (the argument of α): if the exoplanet PA aligns with the direction of the maximal baseline, the contrast will be optimal. However, if a baseline is orthogonal to the planet’s position, the baseline becomes useless. Thus, the simultaneous usage of all baselines is crucial to cover all possible PAs of the exoplanet.

To illustrate this effect, Figure 8 shows the contrast limit using all different baselines of the array as a function of the 2D vector α shown in RA-DEC. To compute the contrast limit, we calculated the S_{ij}/N_{ij} on each projected baseline and summed it as:

$$S/N = \sqrt{\sum_{ij} (S_{ij}/N_{ij})^2}. \quad (72)$$

Then, we estimated the final contrast using a requirement of 3 on the S/N . This clearly shows that the performance of the VLTI is fundamentally under-performing in the North-West direction.

3.2. Limitations of the Inner Working Angle

As detailed in Eq. (73) of Section 4, the reflected light flux from an exoplanet decreases with the square of its distance from the host star. Consequently, the detectability of exoplanets heavily depends on the instrument’s ability to observe companions close to their star. This capability is quantified by the Inner Working Angle (IWA), a critical metric for assessing the effectiveness of astronomical instruments in detecting companions at short separation.

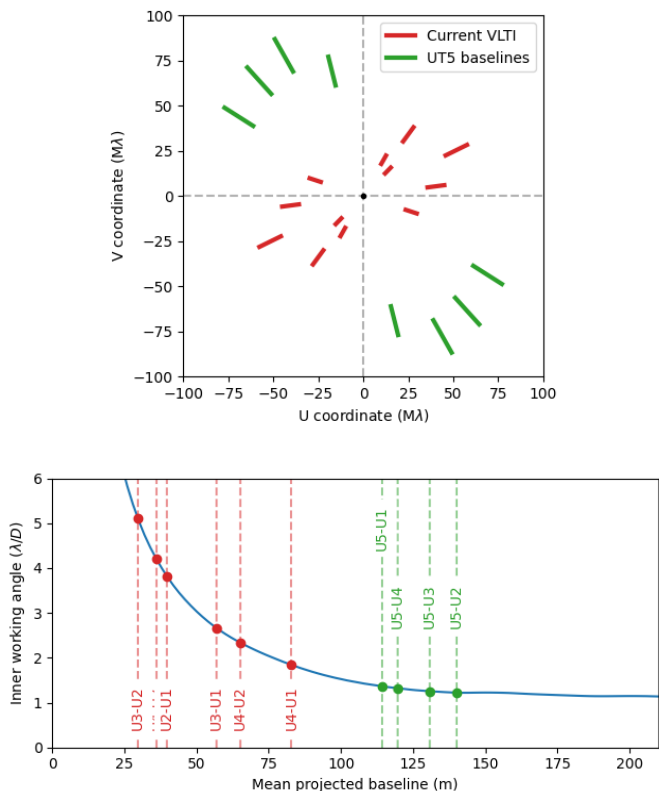


Fig. 7. *Upper panel:* The frequency coverage of the VLTI when observing Proxima Cen passing the meridian is shown in red. The coverage of the current VLTI is confined within an oval oriented towards the North-East direction. The proposed upgrade, with the addition of a new 8 m telescope (highlighted in green), would create four additional baselines extending into the North-West direction. *Lower panel:* Inner Working Angle (IWA) as a function of the PA-averaged projected baseline length $\alpha \cdot \mathbf{B}/|\alpha| = |\mathbf{B}|/\sqrt{2}$. For very long baseline lengths, the IWA is limited by telescope diffraction, approaching one λ/D . However, for most of the VLTI baselines, the IWA is typically limited to several λ/D . The addition of a new telescope would create four new baselines with an IWA only limited by the 8-meter telescope diameter.

The IWA showed in Fig. 8 is influenced by two factors which both reduces the exoplanet signal: $\eta_{\bullet}^{\text{inj}}$ and $\eta_{\bullet}^{\text{proc}}$. The first parameter, $\eta_{\bullet}^{\text{inj}}$, arises from the phase apodization used to reduce the stellar flux. Its impact gets bigger as α becomes close to λ/D (as shown in Figure 4), meaning that the extent of its effect is governed by the diameter D of the individual telescopes of the array.

Conversely, the influence of $\eta_{\bullet}^{\text{proc}}$, depicted in Figure 5, becomes significant when the separation is too small for the oscillatory term $e^{ik\alpha \cdot \mathbf{B}}$ to effectively separate the exoplanet signal from the residual starlight. This starts to occur when the α becomes close to a few $\lambda/\Delta\lambda$ of λ/\mathbf{B} , where \mathbf{B} is the projected baseline.

Hence, the IWA depends both on the diameter of the telescopes and the baseline length, whichever limit comes first. This is illustrated in the lower panel of Fig. 7, which plots the IWA as defined by the angular separation at which the quantity $\eta_{\bullet}^{\text{inj}}\eta_{\bullet}^{\text{proc}}$ equals 1/2. This figure shows the IWA's noticeable increase at shorter baselines (baseline-limited regime) and its stabilization at longer baselines (telescope diameter-limited regime). The red vertical lines represent the lengths of the six existing baselines of the VLTI averaged over all possible orientations. They highlight

that the current VLTI IWA is limited by its baselines, thus not fully capitalizing on the individual telescopes' size. Four additional baselines with projected lengths above 100 meters would enable the observation of exoplanets with a minimal IWA.

3.3. Physical implementation of the Fifth UT

Given the need to both enhance the UV coverage in the North-West direction and increase the baseline lengths for maximizing the Inner Working Angle (IWA), we have devised a proposal for integrating a fifth UT that addresses these challenges without extensive change to the VLTI architecture.

This new telescope could be constructed to the south of UT4, across the road. It would be aligned with the AT J band arm, facilitating the propagation of the beam toward the delay line tunnels. The required delay line for a baseline of approximately 200 meters could be achieved by serially utilizing the two remaining unused delay lines of the VLTI. An aerial view of this proposed setup is presented in Figure 9.

In terms of UV coverage, the four new baselines would ideally complement the existing frequency coverage, as shown by Fig. 7. With these four new baselines, the IWA would also reach optimal levels, approaching the theoretical limit of λ/D . Additionally, this configuration would enhance the contrast limit at many position angles, improving the detectability of exoplanets. As shown in the right panel of Fig. 8, this setup would enable the detection of an exoplanet at a 1 AU distance from a star located 10 parsecs away across all position angles. This setup would also allow for the detection of Proxima Centauri b at its most favorable position angle. The enhancements provided by these additional capabilities are quantified in the subsequent section.

4. Detection rate of reflected light exoplanets

4.1. Simulated orbital realizations

We used the Planetary System database of the NASA Exoplanet Archive³ (Akeson et al. 2013) as our main source of information on the confirmed exoplanets. As of January 25, 2024, it contained a total of 5572 exoplanets. We focused in this study on the 451 known exoplanets within 30 pc.

We applied the methodology of Carrión-González et al. (2021a) and computed 1000 orbital realizations for each of these planets (we refer to Sects. 3 and 4 therein for a more detailed description). Each orbital realization was discretized into 360 orbital positions, at which we computed the planet-star angular separation ($\Delta\theta$) and the brightness of the planet in reflected starlight, which is given by the planet-to-star contrast ratio (F_{\bullet}/F_{\star}). For each orbital position, F_{\bullet}/F_{\star} is computed at a given wavelength (λ) as:

$$\frac{F_{\bullet}}{F_{\star}} = \left(\frac{R_{\bullet}}{r(t)} \right)^2 A_g(\lambda) \Phi(\alpha, \lambda), \quad (73)$$

with R_{\bullet} being the planetary radius, r the distance between the planet and the star, and α the corresponding star-planet-observer phase angle. We assumed for all planets a Lambertian scattering phase law (Φ), and carried out our analysis for geometric albedo (A_g) values of 0.3 and 0.1 (see Sect. 4.2).

When a planet lacked a radius measurement, we computed it using either the mass-radius relationships from Otegi et al. (2020) for rocky and for volatile-rich exoplanets, or the one from

³ <https://exoplanetarchive.ipac.caltech.edu>

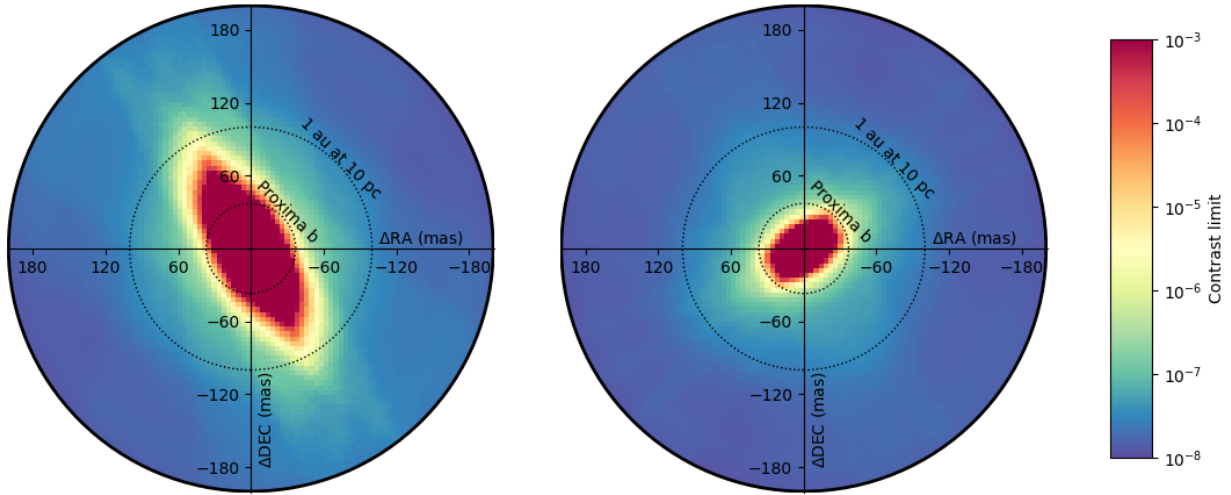


Fig. 8. Contrast limit of a dual-field interferometer using the current four-UT configuration of the VLTI, compared to the proposed five-UT configuration shown in Figure 9.

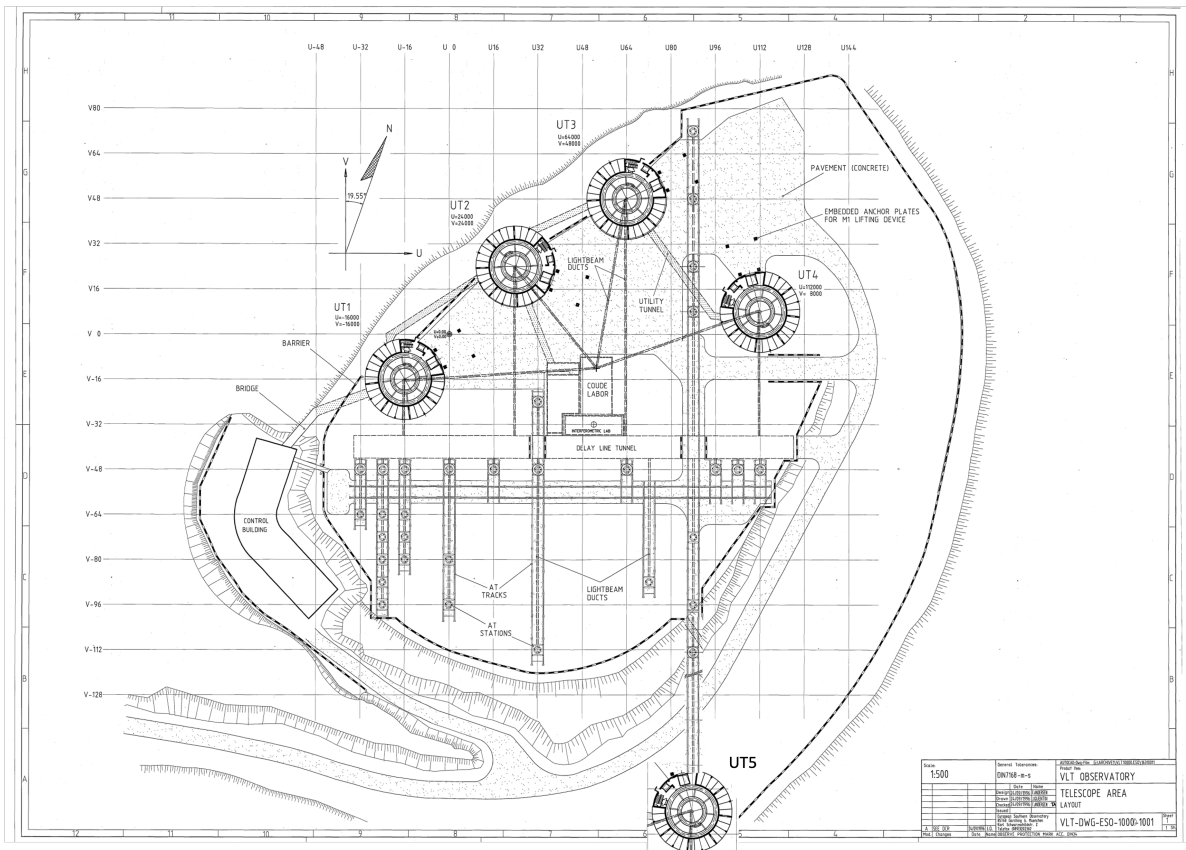


Fig. 9. Aerial view of the proposed extension of the VLTI. The new UT5 telescope would be positioned to the southeast of the platform, on the opposite side of the access road. The beam would be propagated to the VLTI tunnel through the J arm of the existing VLTI/AT interferometer, creating four new baselines with north-south orientations, each approximately 200 meters in length. With a length of 220 meters and an orientation at 154 degrees to the South-East, the UT3-UT4 baseline would be almost orthogonal to the existing long UT1-UT4 baseline giving an optimal UV coverage. The long delay line could be obtained by serializing the two remaining, presently unused, VLTI delay lines.

Hatzes & Rauer (2015) for giant planets. In case of a missing value for the orbital inclination (i) or the argument of periastron of the planet (ω_p), we assumed an isotropic distribution of orbital orientations and drew random values from $\cos(i) \in [-1, 1]$ and $\omega_p \in [0, 2\pi]$ at each orbital realization. Similarly, we drew values for the orbital eccentricity (e) from $e \in [0, 1]$ if it had not

been measured. We assumed that the NASA Exoplanet Archive reports for each planet the argument of periastron of the host star (ω_*), following the radial-velocity convention. Sect. 4.1.1 in Carrión-González et al. (2021a) provides details on the lack of homogeneous criteria to report the planetary argument of pe-

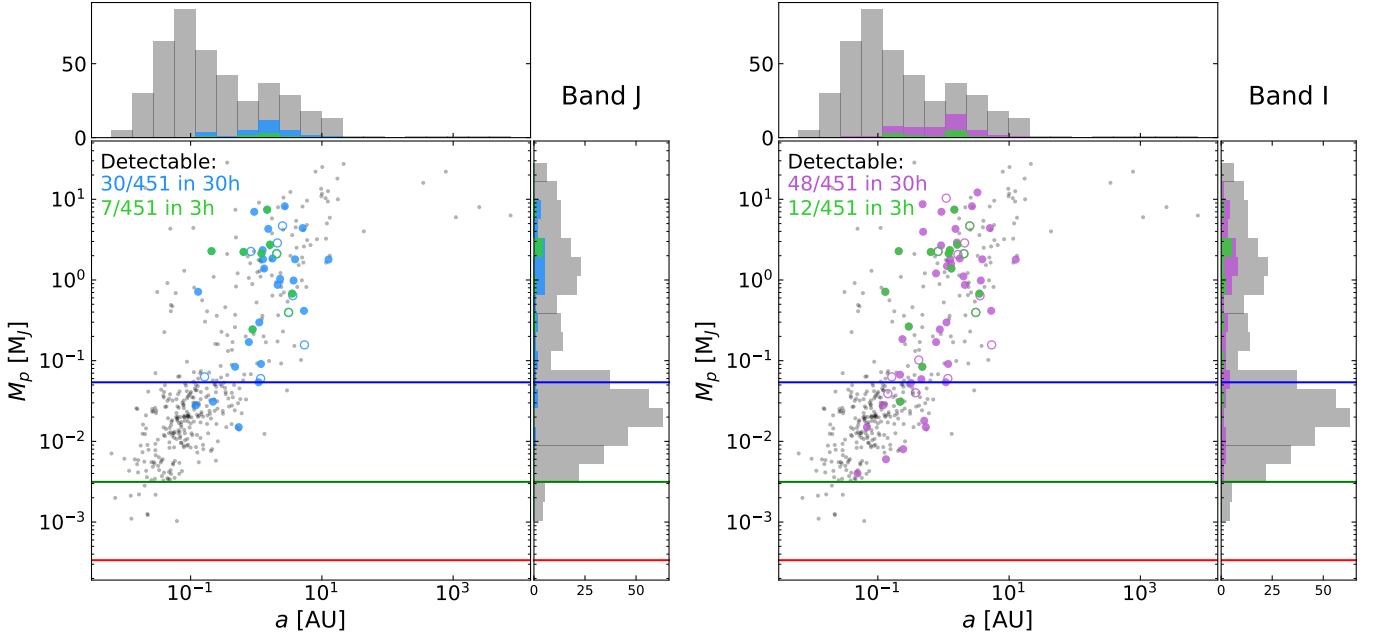


Fig. 10. Detectable exoplanets with the current four-UT configuration with a 100 m baseline (left) at the J band and the proposed five-UT with 200 m baselines (right) at the I band. Blue and purple circles and histograms show the detectable planets in 30 h of integration time in each case, and green ones correspond to planets detectable in 3 h. Empty circles indicate planets that could be detectable by such an instrument but are out of the DEC $\in \{-90^\circ, +30^\circ\}$ interval observable from Paranal, and thus not included in the tally of detectable planets. Grey dots and histograms show the ensemble of known exoplanets within 30 pc. For non-detectable exoplanets, we plot either M_p or $M_p \sin i$ as reported in the NASA Archive. Horizontal lines indicate the masses of Neptune (blue), Earth (green) and Mars (red).

Table 3. Detectability at each spectral band of the exoplanets within 30 pc that are potential targets ($P_{detect} > 25\%$) in at least one band with 3 h of integration time. Both the configurations assuming 4 or 5 telescopes are shown. In all cases, we adopted a value of $A_g = 0.3$ for bands I and J, and $A_g = 0.1$ for H and K. The corresponding targets in 30 h of integration time are displayed in Tables B.1 and B.2.

Planet	d [pc]	a [AU]	M_p [M_J]	P_{detect} [%]	I		J		H		K	
					α_{obs} [deg]	P_{detect} [%]	α_{obs} [deg]	P_{detect} [%]	α_{obs} [deg]	P_{detect} [%]	α_{obs} [deg]	P_{detect} [%]
VLT	HD 62509 b	10.34	1.62	2.74	100.00	$[31^{+26}_{-18}, 127^{+2}_{-5}]$	100.00	$[31^{+26}_{-14}, 123^{+1}_{-2}]$	99.90	$[32^{+25}_{-2}, 101^{+2}_{-2}]$	97.80	$[44^{+11}_{-2}, 86^{+2}_{-3}]$
	eps Eri b	3.20	3.53	0.68	100.00	$[14^{+12}_{-5}, 115^{+1}_{-1}]$	100.00	$[14^{+12}_{-6}, 100^{+6}_{-2}]$	100.00	$[24^{+14}_{-3}, 71^{+9}_{-5}]$	0.00	–
	alf Tau b	20.44	1.47	7.44	100.00	$[28^{+29}_{-6}, 118^{+1}_{-1}]$	100.00	$[37^{+21}_{-5}, 115^{+1}_{-1}]$	49.70	$[61^{+6}_{-4}, 81^{+5}_{-3}]$	0.00	–
	alf Ari b	20.21	1.20	2.13	100.00	$[31^{+28}_{-2}, 105^{+1}_{-1}]$	100.00	$[39^{+20}_{-1}, 98^{+1}_{-2}]$	0.00	–	0.00	–
	GJ 876 b	4.68	0.21	2.28	100.00	$[41^{+1}_{-1}, 97^{+1}_{-1}]$	100.00	$[53^{+0}_{-0}, 94^{+1}_{-1}]$	0.00	–	0.00	–
	GJ 896 A b	6.26	0.64	2.23	71.60	$[53^{+4}_{-1}, 73^{+3}_{-2}]$	99.90	$[47^{+2}_{-2}, 80^{+2}_{-3}]$	0.00	–	0.00	–
	GJ 876 c	4.68	0.13	0.71	100.00	$[46^{+0}_{-0}, 92^{+1}_{-1}]$	0.00	–	0.00	–	0.00	–
	GJ 9066 c	4.47	0.88	0.24	12.70	$[56^{+5}_{-5}, 66^{+5}_{-4}]$	47.60	$[54^{+15}_{-10}, 87^{+2}_{-8}]$	0.00	–	0.00	–
Extended VLT	HD 62509 b	10.34	1.62	2.74	100.00	$[31^{+26}_{-18}, 127^{+2}_{-5}]$	100.00	$[31^{+26}_{-17}, 123^{+2}_{-2}]$	99.90	$[31^{+26}_{-8}, 102^{+3}_{-3}]$	99.30	$[33^{+23}_{-2}, 91^{+3}_{-2}]$
	alf Tau b	20.44	1.47	7.44	100.00	$[28^{+29}_{-10}, 119^{+1}_{-2}]$	100.00	$[29^{+28}_{-5}, 119^{+1}_{-1}]$	99.70	$[44^{+13}_{-5}, 96^{+2}_{-3}]$	43.50	$[62^{+6}_{-4}, 82^{+2}_{-3}]$
	eps Eri b	3.20	3.53	0.68	100.00	$[14^{+12}_{-5}, 113^{+1}_{-2}]$	100.00	$[14^{+12}_{-6}, 108^{+5}_{-2}]$	100.00	$[24^{+14}_{-3}, 71^{+6}_{-4}]$	0.00	–
	alf Ari b	20.21	1.20	2.13	100.00	$[31^{+28}_{-10}, 109^{+1}_{-2}]$	100.00	$[31^{+28}_{-4}, 110^{+1}_{-1}]$	0.00	–	0.00	–
	GJ 876 c	4.68	0.13	0.71	100.00	$[34^{+0}_{-0}, 110^{+0}_{-0}]$	100.00	$[47^{+0}_{-0}, 100^{+1}_{-0}]$	0.00	–	0.00	–
	GJ 876 b	4.68	0.21	2.28	100.00	$[31^{+0}_{-0}, 103^{+1}_{-1}]$	100.00	$[38^{+0}_{-0}, 111^{+1}_{-1}]$	0.00	–	0.00	–
	GJ 896 A b	6.26	0.64	2.23	67.00	$[45^{+4}_{-2}, 79^{+4}_{-1}]$	100.00	$[39^{+2}_{-2}, 88^{+3}_{-3}]$	0.00	–	0.00	–
	HD 27442 b	18.27	1.27	1.81	7.20	$[56^{+2}_{-1}, 63^{+2}_{-2}]$	71.30	$[46^{+2}_{-2}, 66^{+4}_{-5}]$	0.00	–	0.00	–
	nu Oct A b	21.15	1.25	2.34	30.60	$[55^{+5}_{-1}, 70^{+3}_{-4}]$	47.10	$[53^{+5}_{-7}, 68^{+4}_{-4}]$	0.00	–	0.00	–
	61 Vir d	8.50	0.48	0.08	41.20	$[55^{+13}_{-8}, 84^{+16}_{-14}]$	26.60	$[62^{+12}_{-7}, 86^{+17}_{-14}]$	0.00	–	0.00	–
GJ 9066 c	4.47	0.88	0.24	4.90	$[55^{+8}_{-8}, 67^{+5}_{-4}]$	54.50	$[51^{+17}_{-10}, 87^{+14}_{-11}]$	0.00	–	0.00	–	
HD 26965 b	5.04	0.22	0.03	29.70	$[61^{+13}_{-11}, 89^{+13}_{-19}]$	21.80	$[64^{+13}_{-6}, 94^{+8}_{-16}]$	1.20	$[84^{+2}_{-2}, 94^{+1}_{-3}]$	0.00	–	
HD 147513 b	12.90	1.32	1.39	50.30	$[54^{+3}_{-2}, 63^{+3}_{-3}]$	0.00	–	0.00	–	0.00	–	
HD 3651 b	11.13	0.30	0.27	42.70	$[86^{+4}_{-5}, 100^{+2}_{-3}]$	0.00	–	0.00	–	0.00	–	

riatron on catalogues, and its impact for exoplanet detectability studies.

If no value was available for the stellar mass, radius or temperature (M_\star , R_\star , T_\star), we used those in the Planetary Systems Composite Data database of the NASA Exoplanet Archive. Also, if the stellar magnitude at bands I, J, H or K was not reported in

the NASA Exoplanet Archive, we obtained it from the SIMBAD database (Wenger et al. 2000).

This affects in particular the I magnitude, which is unavailable for 198 of the planets within 30 pc. If also unavailable in SIMBAD, we adopted the value of the J magnitude as an ap-

proximation – this however happened for none of the detectable-exoplanet hosts in Table 3.

With the S/N analytical model from Sect. 2, assuming the VLTI parameters used to make Fig. 8 with a projection along the best possible orientation, and adapting in each case for the stellar luminosity, we computed the detectability of the orbital realizations simulated for each exoplanet. A planet is considered detectable at a given orbital position of a given orbital realization if an $S/N = 3$ is achievable in less than 3 h of integration time. The probability of a planet to be detectable (P_{detect}) is given by the number of detectable orbits – those with at least one orbital position detectable – divided by the total number of orbits simulated. As described below, we also explored the number of planets detectable if the integration time is increased to 30 h.

4.2. Detectable exoplanets

We applied our methods to the 451 confirmed exoplanets within 30 pc, and obtained a list of detectable planets at each spectral band. For each planet, the value of A_g will strongly depend on the structure and composition of its atmosphere. In the case of the exoplanets under study here, this information will be a priori completely unknown. For reference, Solar-System bodies have geometrical albedos at spectral bands I, J, H and K ranging from about 0.0 to 0.5, significantly impacted by the presence of clouds and by methane absorption bands in the case of gaseous planets (e.g. Fink & Larson 1979; Madden & Kaltenecker 2018). In agreement with values from Solar System giants, we adopted in Table 3 an albedo of 0.3 at bands I and J, and $A_g = 0.1$ for bands H and K.

In order to build a target list that is statistically robust, we only considered as suitable targets those planets meeting $P_{\text{detect}} > 25\%$. Similarly, we discarded any planet with declination out of the interval $\text{DEC} \in \{-90^\circ, +30^\circ\}$ and thus not observable from Paranal.

Table 3 contains the list of targets and their detectability conditions, and Fig. A.1 shows the simulated orbits for each planet compared to the sensitivity curves of the instrument. For integration times of 3 h, we find 8 exoplanets that are detectable in at least one of the four bands under study with the current VLTI configuration. For the extended VLTI configuration (ie., the current VLTI plus UT5), this count rises to 14 detectable planets. We find that the majority of the detectable targets are long-period planets in the mass range of Jupiter, although the new UT5 can allow to detect planets in the Neptune-mass regime (Fig. 10). These targets, and in particular the lower-mass ones, are detectable mostly at the I and J spectral bands (Table 3), while the expected low-albedos at H and K bands makes them undetectable at such longer wavelengths. Extending the integration time to 30 h increases the tally of detectable planets to 40 with the VLTI and 50 with the extended VLTI (Tables B.1 and B.2). With the new UTs, low-mass planets down to the Earth-like range (e.g. Proxima Cen b) become detectable (see Sect. 4.2.1).

We find wide ranges of observable phase angles (α_{obs}) for several of the exoplanets detectable even in 3 h of integration (Table 3), reaching phases both before and after quadrature ($\alpha = 90^\circ$). These are prime targets for atmospheric characterization, as combining the information of multi-phase observations has been found to significantly improve the atmospheric retrievals in direct imaging (Damiano et al. 2020; Carrión-González et al. 2021b). For 30 h of integration, this list of targets detectable at multiple phase angles increases significantly, including several low-mass planets (Tables B.1 and B.2). In addition, several multi-planet systems have more than one detectable planet of-

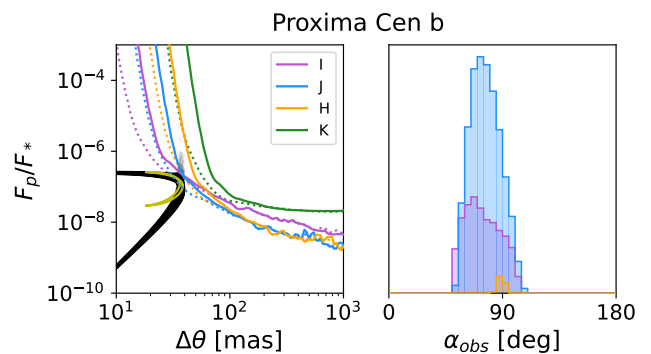


Fig. 11. Detectability conditions for Proxima Cen b with the extended VLTI configuration. Left panel show the simulated orbits (black lines) assuming $A_g = 0.3$, as well as the mean orbital realization (as shown in Figs. 4-6) in yellow. Colored lines show the detectability limits of the interferometer at each spectral band with the VLTI (solid lines) and the extended VLTI (Fig. 9, dotted lines) configurations. In this case, we show the detectability limits for a $S/N = 3$ in 30 h of integration time, instead of 3 h. The histograms on the right panel show the range of α_{obs} at each band.

fering a good opportunity to study the architecture of planetary systems, and the evolution of the planets therein and their atmospheres.

Notably, two promising targets for this instrument in 3 h of integration (HD 62509 b and ϵ Eri b) are potentially detectable as well with the Nancy Grace Roman Space Telescope in reflected starlight (Carrión-González et al. 2021a). Roman will be the first space-based facility capable of directly imaging cold and temperate exoplanets in reflected starlight. It will be launched in late 2026 or 2027, with a mission duration of five years and a potential extension of five more. With the spectral range of Roman’s coronagraph instrument limited to within 575 and 825 nm (Akeson et al. 2019; Zellem et al. 2022), this showcases synergies between both facilities for complementary –and potentially simultaneous– observations in a wider spectral range.

4.2.1. Pushing the instrumental limits: the case of Proxima Cen b

The adopted detectability criteria ($S/N = 3$ in less than 3 h of integration time, $P_{\text{detect}} > 25\%$) ensure the robustness of the target list in Table 3. However, tens of additional known exoplanets that are not included in Table 3 are at the limits of our detectability criteria. These planets could be considered as potential targets for high-risk high-gain observations by increasing the integration time beyond 3 h. Tables B.1 and B.2 showcase the detectable exoplanets ($P_{\text{detect}} > 25\%$) for an integration time of 30 h.

Several temperate low-mass exoplanets are among these, including the habitable-zone super Earths τ Cet e and f, as well as Proxima Cen b, a potentially rocky planet at the habitable zone of our nearest stellar neighbour. We find that for a detection threshold of $S/N = 3$, 30 h of integration would be enough to detect Proxima Cen b with the upgraded VLTI configuration at bands I and J (Fig. 11). The a priori unknown atmospheric properties of the planet will also modify the detectability, and we note that if its albedo is for instance similar to that of Venus (0.45 at band I, 0.4 at band J, Madden & Kaltenecker 2018) the prospects for detecting the planet will be more favourable than reported here.

5. Conclusion and perspectives

In this paper, we have demonstrated that:

1. Dual-field interferometry shows significant potential for detecting exoplanets in reflected light, positioning it as a competitive technique alongside cross-correlation methods used with the ELT or space-based coronagraphy.
2. The primary limitation of this technique is shot noise from stellar light, which can be effectively mitigated through the combined use of phase apodization and a high-performance AO system.
3. Sensitivity is enhanced at shorter wavelengths, provided the AO system performs well (Strehl ratio above 50%). Furthermore, planets are expected to exhibit higher geometrical albedo at these wavelengths, further improving detectability.
4. The inner working angle is constrained by both the telescope diameter and the baseline length, with optimal performance achieved when the projected baseline length is ≥ 10 times the telescope diameter.

The proposed addition of a new Unit Telescope to the South of the VLTI platform would greatly enhance the VLTI's efficiency. This upgrade would not only increase the number of baselines > 100 meters by five but it would also double the angular resolution and expand the UV coverage to include the North-West direction. Such improvements would significantly boost the VLTI's capability, offering the best opportunity to detect signals from temperate, Earth-mass exoplanets like Proxima Centauri b in reflected light.

As of now, no direct-imaging observations of exoplanets in reflected starlight have been performed, as they require sensitivity levels out of reach for current facilities. The proposed extension of the VLTI will join a handful of other missions and concepts capable of reaching this sensitivity in the near- and mid-term future, such as the PCS instrument envisioned for the ELT (Kasper et al. 2021), the Roman Space Telescope's Coronagraph Instrument technology demonstrator (Bailey et al. 2023), and the future Habitable Worlds Observatory. This will enable the characterization of the poorly-studied population of cold and temperate long-period exoplanets, including in the case of an extended VLTI several low-mass temperate targets.

Additionally, the increased resolution to the VLTI would also help numerous other science cases that are fundamental to the astronomical community. Thanks to a better astrometry, it would be possible to detect exomoons, to measure the masses of galactic stellar black holes (Gaia Collaboration et al. 2024), as well as high redshift super-massive black holes (Abuter et al. 2024). The extended UV coverage would also bring increased imaging capabilities to the UTs, that could be fundamental to image faint objects, like protoplanets (Wang et al. 2021) and AGN's nuclei (GRAVITY Collaboration et al. 2020b).

Acknowledgements. This research made use of HCIPy, an open-source object-oriented framework written in Python for performing end-to-end simulations of high-contrast imaging instruments (Por et al. 2018). SL acknowledges the support of the French "Agence Nationale de la Recherche" (ANR), under grants ANR-21-CE31-0017 (project ExoVLTI) and ANR-22-EXOR-0005 (PEPR Origins). The authors thank Dr. A. Kellerer and Dr. G. Bourdarot for their thorough proofreading and extensive review of the mathematical formulations.

References

Abuter, R., Allouche, F., Amorim, A., et al. 2024, *Nature*, 627, 281
 Akeson, R., Armus, L., Bachelet, E., et al. 2019, arXiv e-prints, arXiv:1902.05569

Akeson, R. L., Chen, X., Ciardi, D., et al. 2013, *PASP*, 125, 989
 Bailey, V. P., Bendek, E., Monacelli, B., et al. 2023, in *Society of Photo-Optical Instrumentation Engineers (SPIE) Conference Series*, Vol. 12680, Society of Photo-Optical Instrumentation Engineers (SPIE) Conference Series, 126800T
 Beuzit, J.-L., Vigan, A., Mouillet, D., et al. 2019, *Astronomy & Astrophysics*, 631, A155
 Bracewell, R. N. 1978, *Nature*, 274, 780
 Carrión-González, Ó., García Muñoz, A., Santos, N. C., et al. 2021a, *A&A*, 651, A7
 Carrión-González, Ó., García Muñoz, A., Santos, N. C., et al. 2021b, *A&A*, 655, A92
 Chingaipe, P. M., Martinache, F., Cvetojevic, N., et al. 2023, *Astronomy & Astrophysics*, 676, A43
 Damiano, M., Hu, R., & Hildebrandt, S. R. 2020, *AJ*, 160, 206
 Fink, U. & Larson, H. P. 1979, *ApJ*, 233, 1021
 Fusco, T., Sauvage, J. F., Mouillet, D., et al. 2016, 9909, 99090U
 Gaia Collaboration, Panuzzo, P., Mazeh, T., et al. 2024, *A&A*, 686, L2
 Gardner, T., Monnier, J. D., Fekel, F. C., et al. 2018, *ApJ*, 855, 1
 Gaudi, B. S., Seager, S., Mennesson, B., et al. 2018, arXiv e-prints, arXiv:1809.09674
 Gravity Collaboration, Abuter, R., Accardo, M., et al. 2017, *Astronomy and Astrophysics*, 602, A94
 Gravity+ Collaboration, Abuter, R., Alarcon, P., et al. 2022, *The Messenger*, 189, 17
 GRAVITY Collaboration, Lacour, S., Nowak, M., et al. 2019, *Astronomy and Astrophysics*, 623, L11
 GRAVITY Collaboration, Nowak, M., Lacour, S., et al. 2020a, *Astronomy and Astrophysics*, 633, A110
 GRAVITY Collaboration, Pfuhl, O., Davies, R., et al. 2020b, *A&A*, 634, A1
 Guyon, O. 2005, *The Astrophysical Journal*, 629, 592
 Haffert, S. Y., Por, E. H., Keller, C. U., et al. 2020, *Astronomy and Astrophysics*, 635, A56
 Hatzes, A. P. & Rauer, H. 2015, *ApJ*, 810, L25
 Hinkley, S., Lacour, S., Marleau, G. D., et al. 2023, *Astronomy and Astrophysics*, 671, L5
 Kasper, M., Cerpa Urta, N., Pathak, P., et al. 2021, *The Messenger*, 182, 38
 Lustig-Yaeger, J., Meadows, V. S., & Lincowski, A. P. 2019, *The Astronomical Journal*, 158, 27
 Madden, J. H. & Kaltenecker, L. 2018, *Astrobiology*, 18, 1559
 Marois, C., Lafreniere, D., Doyon, R., Macintosh, B., & Nadeau, D. 2006, *The Astrophysical Journal*, 641, 556
 Martinache, F. & Ireland, M. J. 2018, *Astronomy & Astrophysics*, 619, A87
 Mennesson, B., Gaudi, S., Seager, S., et al. 2016, in *Society of Photo-Optical Instrumentation Engineers (SPIE) Conference Series*, Vol. 9904, *Space Telescopes and Instrumentation 2016: Optical, Infrared, and Millimeter Wave*, ed. H. A. MacEwen, G. G. Fazio, M. Lystrup, N. Batalha, N. Siegler, & E. C. Tong, 99040L
 Nowak, M., Lacour, S., Lagrange, A. M., et al. 2020, *Astronomy and Astrophysics*, 642, L2
 Otegi, J. F., Bouchy, F., & Helled, R. 2020, *A&A*, 634, A43
 Palle, E., Biazzo, K., Bolmont, E., et al. 2023, arXiv e-prints, arXiv:2311.17075
 Por, E. H. 2017, in *Techniques and Instrumentation for Detection of Exoplanets VIII*, Vol. 10400 (SPIE), 236–247
 Por, E. H. 2020, *The Astrophysical Journal*, 888, 127
 Por, E. H., Haffert, S. Y., Radhakrishnan, V. M., et al. 2018, in *Adaptive Optics Systems VI*, Vol. 10703 (SPIE), 1112–1125
 Potier, A., Mazoyer, J., Wahhaj, Z., et al. 2022, *Astronomy and Astrophysics*, 665, A136
 Poiré, N., Winterhalder, T. O., Le Bouquin, J. B., et al. 2024, arXiv e-prints, arXiv:2406.04003
 Quanz, S. P., Ottiger, M., Fontanet, E., et al. 2021, arXiv e-prints, arXiv:2101.07500
 Racine, R., Walker, G. A. H., Nadeau, D., Doyon, R., & Marois, C. 1999, *Publications of the Astronomical Society of the Pacific*, 111, 587
 Rouan, D., Riaud, P., Boccaletti, A., Clénet, Y., & Labeysrie, A. 2000, *Publications of the Astronomical Society of the Pacific*, 112, 1479
 Ruffio, J.-B., Horstman, K., Mawet, D., et al. 2023, *AJ*, 165, 113
 Ruffio, J.-B., Macintosh, B., Konopacky, Q. M., et al. 2019, *AJ*, 158, 200
 Snellen, I., de Kok, R., Birkby, J. L., et al. 2015, *A&A*, 576, A59
 Snellen, I. A. G., de Kok, R. J., le Poole, R., Brogi, M., & Birkby, J. 2013, *ApJ*, 764, 182
 Spergel, D., Gehrels, N., Baltay, C., et al. 2015, arXiv e-prints, arXiv:1503.03757
 The LUVOIR Team. 2018, arXiv e-prints, arXiv:1809.09668
 Wang, J. J., Vigan, A., Lacour, S., et al. 2021, *AJ*, 161, 148
 Wenger, M., Ochsenein, F., Egret, D., et al. 2000, *A&AS*, 143, 9
 Woillez, J. & Lacour, S. 2013, *The Astrophysical Journal*, 764, 109
 Zellem, R. T., Nemati, B., Gonzalez, G., et al. 2022, in *Society of Photo-Optical Instrumentation Engineers (SPIE) Conference Series*, Vol. 12180, *Space Telescopes and Instrumentation 2022: Optical, Infrared, and Millimeter Wave*, ed. L. E. Coyle, S. Matsuura, & M. D. Perrin, 121801Z

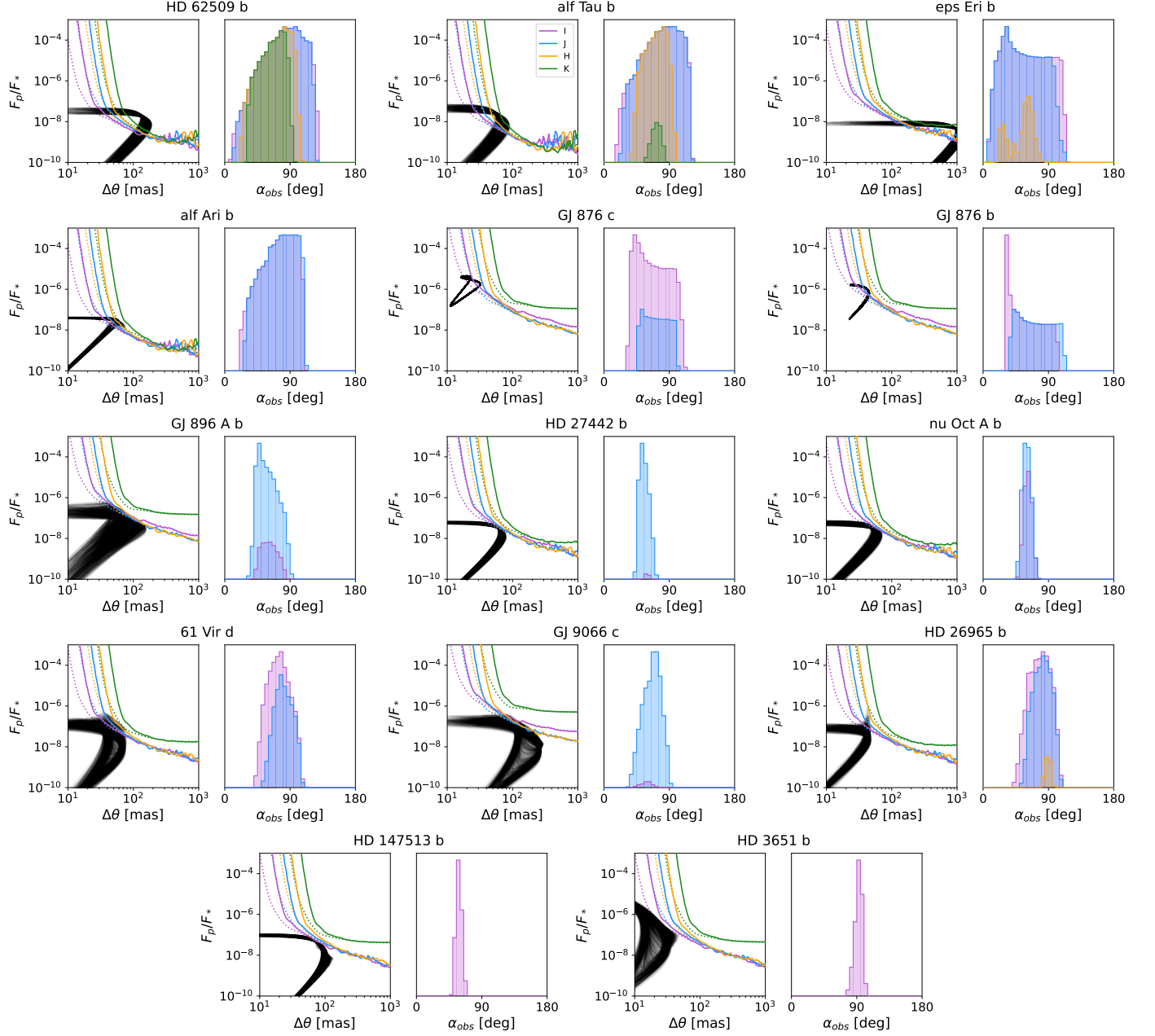
Appendix A: Simulated orbits and detectability of known exoplanets


Fig. A.1. Detectability conditions for the targets with $P_{detect} > 25\%$ in 3 h of integration. Left panels show the simulated orbits of each planet (black lines) assuming $A_g = 0.3$. Colored lines show the detectability limits of the interferometer at each spectral band with the current VLTI (solid lines) and the extended VLTI (dotted lines) baselines, for a $S/N = 3$ in 3 h of integration. The histograms on the right panels show the range of α_{obs} at each band with the extended VLTI configuration.

Appendix B: Detectable targets in 30 h of integration time

Table B.1. List of detectable targets as in Table 3, but for an integration time of 30 h with the current VLTI configuration.

Planet	d [pc]	a [AU]	M_p [M_J]	P_{detect} [%]	I	J	H	K			
					α_{obs} [deg]	P_{detect} [%]	α_{obs} [deg]	P_{detect} [%]	α_{obs} [deg]	P_{detect} [%]	
HD 62509 b	10.34	1.62	2.74	100.00	$[31^{+26}_{-20}, 140^{+1}_{-17}]$	100.00	$[31^{+26}_{-17}, 137^{+1}_{-14}]$	100.00	$[31^{+26}_{-11}, 123^{+1}_{-1}]$	100.00	$[31^{+26}_{-5}, 115^{+1}_{-1}]$
eps Eri b	3.20	3.53	0.68	100.00	$[14^{+12}_{-9}, 130^{+2}_{-2}]$	100.00	$[14^{+12}_{-9}, 128^{+2}_{-2}]$	100.00	$[14^{+12}_{-5}, 92^{+16}_{-3}]$	97.30	$[16^{+9}_{-2}, 47^{+5}_{-1}]$
alf Tau b	20.44	1.47	7.44	100.00	$[28^{+29}_{-8}, 133^{+1}_{-10}]$	100.00	$[34^{+24}_{-2}, 130^{+1}_{-1}]$	100.00	$[47^{+11}_{-7}, 112^{+2}_{-4}]$	62.70	$[64^{+10}_{-7}, 96^{+2}_{-3}]$
alf Ari b	20.21	1.20	2.13	100.00	$[31^{+28}_{-11}, 124^{+1}_{-1}]$	100.00	$[31^{+28}_{-2}, 117^{+1}_{-1}]$	99.50	$[50^{+9}_{-2}, 84^{+2}_{-2}]$	0.00	–
GJ 896 A b	6.26	0.64	2.23	100.00	$[24^{+14}_{-3}, 111^{+1}_{-1}]$	100.00	$[26^{+12}_{-3}, 113^{+1}_{-1}]$	87.10	$[54^{+3}_{-3}, 71^{+4}_{-5}]$	0.00	–
GJ 9066 c	4.47	0.88	0.24	98.30	$[38^{+22}_{-3}, 99^{+7}_{-10}]$	100.00	$[35^{+24}_{-8}, 106^{+8}_{-8}]$	40.70	$[57^{+13}_{-10}, 84^{+2}_{-4}]$	0.00	–
nu Oct A b	21.15	1.25	2.34	100.00	$[34^{+22}_{-3}, 106^{+2}_{-2}]$	100.00	$[43^{+14}_{-4}, 101^{+2}_{-2}]$	0.00	–	0.00	–
bet Pic c	19.74	2.72	8.20	100.00	$[30^{+2}_{-2}, 98^{+3}_{-3}]$	100.00	$[43^{+4}_{-4}, 84^{+5}_{-6}]$	0.00	–	0.00	–
HD 27442 b	18.27	1.27	1.81	100.00	$[31^{+25}_{-3}, 106^{+1}_{-1}]$	100.00	$[36^{+19}_{-2}, 105^{+1}_{-1}]$	0.00	–	0.00	–
HD 160691 b	15.60	1.52	4.30	100.00	$[30^{+1}_{-0}, 99^{+2}_{-2}]$	100.00	$[40^{+2}_{-1}, 88^{+2}_{-5}]$	0.00	–	0.00	–
HD 147513 b	12.90	1.32	1.39	100.00	$[29^{+28}_{-3}, 106^{+1}_{-1}]$	100.00	$[38^{+19}_{-1}, 100^{+1}_{-1}]$	0.00	–	0.00	–
GJ 876 c	4.68	0.13	0.71	100.00	$[40^{+0}_{-0}, 114^{+0}_{-0}]$	100.00	$[68^{+1}_{-1}, 81^{+1}_{-1}]$	0.00	–	0.00	–
GJ 876 b	4.68	0.21	2.28	100.00	$[31^{+0}_{-0}, 120^{+0}_{-0}]$	100.00	$[45^{+0}_{-0}, 117^{+0}_{-0}]$	0.00	–	0.00	–
GJ 832 b	4.96	3.70	0.98	100.00	$[39^{+2}_{-2}, 82^{+2}_{-2}]$	100.00	$[39^{+2}_{-2}, 93^{+1}_{-1}]$	0.00	–	0.00	–
7 CMa c	19.81	2.12	0.87	100.00	$[25^{+0}_{-0}, 106^{+1}_{-1}]$	100.00	$[30^{+1}_{-1}, 105^{+1}_{-1}]$	0.00	–	0.00	–
7 CMa b	19.80	1.77	1.85	100.00	$[26^{+1}_{-1}, 105^{+1}_{-1}]$	100.00	$[32^{+1}_{-1}, 104^{+1}_{-1}]$	0.00	–	0.00	–
HD 160691 e	15.60	0.93	7.00	99.70	$[38^{+13}_{-2}, 97^{+2}_{-2}]$	93.90	$[54^{+10}_{-8}, 86^{+2}_{-2}]$	0.00	–	0.00	–
tau Cet e	3.60	0.54	0.01	94.70	$[41^{+18}_{-7}, 95^{+13}_{-17}]$	87.00	$[44^{+16}_{-8}, 94^{+12}_{-13}]$	8.00	$[74^{+8}_{-7}, 94^{+6}_{-15}]$	2.80	$[82^{+3}_{-4}, 93^{+4}_{-5}]$
HD 114613 b	20.28	5.33	0.41	87.20	$[37^{+12}_{-2}, 79^{+9}_{-12}]$	96.90	$[45^{+11}_{-5}, 77^{+3}_{-5}]$	0.00	–	0.00	–
61 Vir d	8.50	0.48	0.08	98.40	$[46^{+13}_{-6}, 98^{+10}_{-12}]$	78.10	$[59^{+9}_{-6}, 96^{+11}_{-12}]$	3.50	$[83^{+4}_{-4}, 100^{+1}_{-4}]$	0.00	–
HD 190360 b	16.01	3.90	1.80	100.00	$[34^{+1}_{-1}, 76^{+3}_{-3}]$	56.30	$[61^{+6}_{-8}, 75^{+4}_{-11}]$	0.00	–	0.00	–
HD 26965 b	5.04	0.22	0.03	97.40	$[48^{+12}_{-7}, 96^{+11}_{-11}]$	45.20	$[62^{+9}_{-5}, 91^{+13}_{-13}]$	0.70	$[86^{+3}_{-1}, 93^{+1}_{-3}]$	0.00	–
GJ 649 b	10.38	1.11	0.30	62.20	$[45^{+15}_{-5}, 82^{+3}_{-4}]$	72.20	$[45^{+15}_{-8}, 87^{+2}_{-5}]$	0.00	–	0.00	–
55 Cnc f	12.59	0.77	0.17	88.00	$[47^{+12}_{-7}, 92^{+14}_{-12}]$	34.00	$[60^{+8}_{-6}, 91^{+9}_{-13}]$	0.00	–	0.00	–
GJ 887 c	3.29	0.12	0.03	76.90	$[53^{+14}_{-9}, 93^{+11}_{-12}]$	42.60	$[63^{+15}_{-11}, 90^{+12}_{-13}]$	1.70	$[83^{+8}_{-6}, 90^{+5}_{-7}]$	0.10	$[89^{+0}_{-0}, 89^{+0}_{-0}]$
HD 10647 b	17.34	2.02	1.11	99.00	$[37^{+22}_{-1}, 88^{+1}_{-2}]$	19.70	$[58^{+3}_{-3}, 66^{+2}_{-1}]$	0.00	–	0.00	–
HD 192310 c	8.80	1.18	0.09	61.30	$[51^{+14}_{-10}, 90^{+14}_{-14}]$	51.00	$[53^{+14}_{-10}, 90^{+15}_{-14}]$	5.00	$[77^{+4}_{-6}, 92^{+2}_{-11}]$	0.00	–
HD 39091 b	18.27	3.29	12.16	99.20	$[49^{+3}_{-2}, 75^{+3}_{-4}]$	0.00	–	0.00	–	0.00	–
HR 810 b	17.32	0.92	2.69	99.10	$[43^{+14}_{-2}, 91^{+2}_{-2}]$	0.00	–	0.00	–	0.00	–
70 Vir b	17.90	0.48	8.70	98.90	$[54^{+8}_{-2}, 94^{+1}_{-2}]$	0.00	–	0.00	–	0.00	–
HD 19994 b	22.52	1.31	1.58	93.10	$[52^{+3}_{-2}, 77^{+2}_{-3}]$	0.00	–	0.00	–	0.00	–
HD 140901 c	15.25	12.61	1.79	35.20	$[43^{+10}_{-4}, 62^{+11}_{-11}]$	56.40	$[57^{+5}_{-5}, 65^{+5}_{-5}]$	0.00	–	0.00	–
tau Cet h	3.60	0.24	0.01	60.30	$[55^{+8}_{-6}, 78^{+21}_{-8}]$	19.10	$[64^{+11}_{-8}, 93^{+9}_{-14}]$	1.40	$[83^{+2}_{-1}, 92^{+3}_{-5}]$	0.20	$[88^{+0}_{-0}, 92^{+0}_{-0}]$
GJ 849 b	8.80	2.31	1.03	0.00	–	75.70	$[38^{+1}_{-1}, 51^{+4}_{-4}]$	0.00	–	0.00	–
HD 60532 c	25.98	1.60	2.91	70.10	$[55^{+3}_{-2}, 69^{+3}_{-3}]$	0.00	–	0.00	–	0.00	–
HD 160691 c	15.60	5.10	4.40	34.20	$[47^{+9}_{-15}, 97^{+3}_{-19}]$	35.90	$[46^{+14}_{-5}, 85^{+4}_{-7}]$	0.00	–	0.00	–
GJ 229 b	5.76	1.09	0.05	30.10	$[59^{+13}_{-10}, 82^{+14}_{-13}]$	32.70	$[57^{+13}_{-9}, 86^{+15}_{-15}]$	4.20	$[77^{+3}_{-5}, 90^{+8}_{-10}]$	0.00	–
HD 102365 b	9.29	0.46	0.06	42.60	$[56^{+15}_{-9}, 89^{+13}_{-13}]$	17.30	$[67^{+10}_{-8}, 88^{+7}_{-13}]$	0.00	–	0.00	–
HD 3651 b	11.13	0.30	0.27	52.80	$[92^{+4}_{-3}, 110^{+4}_{-7}]$	1.10	$[94^{+4}_{-2}, 96^{+3}_{-3}]$	0.00	–	0.00	–
61 Vir c	8.50	0.22	0.07	40.00	$[67^{+6}_{-5}, 92^{+12}_{-12}]$	0.00	–	0.00	–	0.00	–

Table B.2. List of detectable targets as in Table 3, but for an integration time of 30 h with the extended VLTI configuration.

Planet	d [pc]	a [AU]	M_p [M_J]	P_{detect} [%]	I	J	H	K
					α_{obs} [deg]	P_{detect} [%]	α_{obs} [deg]	P_{detect} [%]
alf Tau b	20.44	1.47	7.44	100.00	$[28^{+29}_{-13}, 134^{+1}_{-12}]$	$[28^{+29}_{-8}, 134^{+1}_{-11}]$	$[36^{+22}_{-5}, 120^{+1}_{-2}]$	$[49^{+10}_{-7}, 111^{+2}_{-4}]$
HD 62509 b	10.34	1.62	2.74	100.00	$[31^{+26}_{-21}, 140^{+1}_{-17}]$	$[31^{+26}_{-20}, 138^{+1}_{-15}]$	$[31^{+26}_{-15}, 124^{+1}_{-3}]$	$[31^{+26}_{-10}, 118^{+1}_{-2}]$
eps Eri b	3.20	3.53	0.68	100.00	$[14^{+12}_{-9}, 126^{+5}_{-2}]$	$[14^{+12}_{-9}, 126^{+2}_{-2}]$	$[14^{+12}_{-5}, 100^{+4}_{-3}]$	$[17^{+9}_{-2}, 49^{+5}_{-13}]$
alf Ari b	20.21	1.20	2.13	100.00	$[31^{+28}_{-16}, 128^{+1}_{-7}]$	$[31^{+28}_{-10}, 126^{+1}_{-5}]$	$[36^{+23}_{-1}, 104^{+1}_{-2}]$	$[62^{+3}_{-4}, 75^{+4}_{-4}]$
GJ 896 A b	6.26	0.64	2.23	100.00	$[21^{+16}_{-3}, 113^{+1}_{-2}]$	$[22^{+16}_{-4}, 116^{+2}_{-2}]$	$[39^{+4}_{-2}, 86^{+5}_{-3}]$	0.00
GJ 876 b	4.68	0.21	2.28	100.00	$[31^{+0}_{-0}, 125^{+1}_{-1}]$	$[31^{+0}_{-0}, 126^{+0}_{-0}]$	$[52^{+0}_{-0}, 101^{+1}_{-1}]$	0.00
HD 27442 b	18.27	1.27	1.81	100.00	$[30^{+26}_{-8}, 108^{+1}_{-1}]$	$[30^{+26}_{-6}, 109^{+1}_{-1}]$	$[55^{+3}_{-2}, 72^{+3}_{-4}]$	0.00
GJ 9066 c	4.47	0.88	0.24	97.80	$[37^{+24}_{-10}, 99^{+7}_{-11}]$	$[33^{+27}_{-11}, 106^{+7}_{-8}]$	$[53^{+15}_{-12}, 88^{+2}_{-11}]$	0.00
61 Vir d	8.50	0.48	0.08	100.00	$[36^{+22}_{-5}, 103^{+8}_{-6}]$	$[46^{+12}_{-3}, 101^{+10}_{-9}]$	$[74^{+4}_{-6}, 95^{+7}_{-10}]$	0.00
HD 26965 b	5.04	0.22	0.03	100.00	$[35^{+25}_{-4}, 101^{+10}_{-9}]$	$[48^{+12}_{-5}, 100^{+9}_{-9}]$	$[76^{+7}_{-6}, 95^{+4}_{-11}]$	0.10
nu Oct A b	21.15	1.25	2.34	100.00	$[30^{+26}_{-7}, 109^{+2}_{-2}]$	$[34^{+23}_{-4}, 109^{+2}_{-2}]$	$[61^{+1}_{-2}, 68^{+2}_{-2}]$	0.00
bet Pic c	19.74	2.72	8.20	100.00	$[25^{+3}_{-3}, 97^{+3}_{-3}]$	$[33^{+5}_{-5}, 87^{+4}_{-4}]$	–	0.00
HD 160691 b	15.60	1.52	4.30	100.00	$[30^{+0}_{-0}, 103^{+4}_{-6}]$	$[32^{+3}_{-3}, 94^{+3}_{-3}]$	0.00	0.00
HD 147513 b	12.90	1.32	1.39	100.00	$[29^{+28}_{-10}, 106^{+1}_{-1}]$	$[29^{+28}_{-2}, 102^{+1}_{-1}]$	0.00	0.00
GJ 876 c	4.68	0.13	0.71	100.00	$[31^{+0}_{-0}, 124^{+0}_{-0}]$	$[39^{+0}_{-0}, 113^{+0}_{-0}]$	0.00	0.00
GJ 832 b	4.96	3.70	0.98	100.00	$[39^{+2}_{-2}, 70^{+8}_{-4}]$	$[39^{+2}_{-2}, 89^{+2}_{-2}]$	0.00	0.00
7 CMa c	19.81	2.12	0.87	100.00	$[20^{+1}_{-1}, 106^{+1}_{-1}]$	$[22^{+0}_{-0}, 107^{+1}_{-1}]$	0.00	0.00
7 CMa b	19.80	1.77	1.85	100.00	$[20^{+1}_{-1}, 105^{+1}_{-1}]$	$[24^{+0}_{-0}, 107^{+1}_{-1}]$	0.00	0.00
HD 160691 e	15.60	0.93	7.00	100.00	$[30^{+14}_{-0}, 103^{+4}_{-8}]$	$[40^{+5}_{-4}, 92^{+6}_{-2}]$	0.00	0.00
70 Vir b	17.90	0.48	8.70	100.00	$[41^{+16}_{-2}, 105^{+1}_{-2}]$	$[63^{+7}_{-3}, 92^{+2}_{-2}]$	0.00	0.00
HR 810 b	17.32	0.92	2.69	99.60	$[32^{+25}_{-3}, 96^{+1}_{-1}]$	$[46^{+10}_{-3}, 86^{+2}_{-2}]$	0.00	0.00
tau Cet e	3.60	0.54	0.01	94.40	$[42^{+18}_{-10}, 94^{+13}_{-17}]$	$[42^{+18}_{-8}, 94^{+12}_{-14}]$	$[72^{+9}_{-8}, 93^{+7}_{-14}]$	3.80
GJ 887 c	3.29	0.12	0.03	94.10	$[43^{+20}_{-9}, 101^{+10}_{-10}]$	$[53^{+17}_{-10}, 99^{+9}_{-12}]$	$[76^{+12}_{-11}, 90^{+8}_{-13}]$	0.70
HD 10647 b	17.34	2.02	1.11	98.50	$[34^{+25}_{-7}, 88^{+2}_{-2}]$	$[48^{+4}_{-3}, 74^{+3}_{-3}]$	0.00	0.00
HD 19994 b	22.52	1.31	1.58	97.20	$[37^{+18}_{-2}, 84^{+2}_{-2}]$	$[51^{+3}_{-3}, 71^{+3}_{-3}]$	0.00	0.00
tau Cet h	3.60	0.24	0.01	95.80	$[47^{+12}_{-6}, 82^{+13}_{-8}]$	$[51^{+10}_{-5}, 79^{+16}_{-9}]$	$[79^{+3}_{-5}, 94^{+4}_{-14}]$	0.80
HD 114613 b	20.28	5.33	0.41	86.70	$[37^{+11}_{-7}, 79^{+9}_{-12}]$	$[42^{+14}_{-4}, 76^{+4}_{-4}]$	0.00	0.00
55 Cnc f	12.59	0.77	0.17	96.50	$[39^{+18}_{-9}, 95^{+12}_{-13}]$	$[47^{+12}_{-6}, 86^{+17}_{-15}]$	0.00	0.00
GJ 649 b	10.38	1.11	0.30	61.00	$[43^{+16}_{-6}, 81^{+3}_{-4}]$	$[43^{+15}_{-9}, 91^{+2}_{-9}]$	0.00	0.00
HD 190360 b	16.01	3.90	1.80	100.00	$[34^{+1}_{-1}, 77^{+2}_{-1}]$	$[62^{+4}_{-4}, 74^{+4}_{-4}]$	0.00	0.00
tau Cet g	3.60	0.13	0.01	100.00	$[45^{+13}_{-3}, 86^{+9}_{-6}]$	$[65^{+7}_{-5}, 85^{+13}_{-8}]$	$[85^{+1}_{-0}, 93^{+1}_{-1}]$	0.10
Proxima Cen b	1.30	0.05	0.00	27.80	$[59^{+14}_{-6}, 77^{+15}_{-10}]$	$[61^{+5}_{-4}, 85^{+9}_{-5}]$	$[85^{+2}_{-1}, 93^{+1}_{-4}]$	0.00
HD 3651 b	11.13	0.30	0.27	100.00	$[71^{+6}_{-5}, 116^{+5}_{-5}]$	$[98^{+5}_{-4}, 112^{+3}_{-6}]$	0.00	0.00
61 Vir c	8.50	0.22	0.07	99.30	$[50^{+10}_{-5}, 101^{+9}_{-10}]$	$[73^{+5}_{-5}, 98^{+6}_{-8}]$	0.00	0.00
HD 192310 c	8.80	1.18	0.09	59.30	$[52^{+14}_{-10}, 90^{+14}_{-14}]$	$[51^{+16}_{-11}, 91^{+15}_{-15}]$	$[76^{+5}_{-5}, 97^{+2}_{-16}]$	0.00
HD 102365 b	9.29	0.46	0.06	60.80	$[51^{+16}_{-11}, 92^{+13}_{-15}]$	$[56^{+15}_{-10}, 89^{+13}_{-13}]$	$[79^{+4}_{-4}, 88^{+5}_{-8}]$	0.00
HD 39091 b	18.27	3.29	12.16	100.00	$[42^{+1}_{-1}, 82^{+2}_{-2}]$	–	0.00	0.00
HD 60532 b	25.98	0.77	1.21	99.90	$[43^{+15}_{-1}, 89^{+2}_{-2}]$	0.00	0.00	0.00
HD 60532 c	25.98	1.60	2.91	95.60	$[46^{+6}_{-1}, 78^{+2}_{-2}]$	0.00	0.00	0.00
GJ 3021 b	17.56	0.49	3.95	84.80	$[73^{+5}_{-3}, 93^{+1}_{-2}]$	0.00	0.00	0.00
HD 140901 c	15.25	12.61	1.79	34.50	$[43^{+10}_{-4}, 62^{+11}_{-12}]$	$[57^{+5}_{-10}, 64^{+5}_{-5}]$	0.00	0.00
GJ 849 b	8.80	2.31	1.03	0.00	–	$[39^{+1}_{-1}, 50^{+3}_{-3}]$	0.00	0.00
HD 160691 c	15.60	5.10	4.40	36.50	$[48^{+9}_{-15}, 97^{+8}_{-20}]$	$[45^{+11}_{-10}, 85^{+11}_{-7}]$	0.00	0.00
GJ 229 b	5.76	1.09	0.05	28.60	$[60^{+13}_{-11}, 82^{+14}_{-13}]$	$[54^{+16}_{-9}, 83^{+18}_{-15}]$	$[76^{+4}_{-6}, 89^{+8}_{-10}]$	0.50
55 Cnc c	12.59	0.24	0.18	70.70	$[62^{+8}_{-5}, 96^{+10}_{-8}]$	0.00	0.00	0.00
HD 192310 b	8.80	0.32	0.05	43.10	$[48^{+9}_{-5}, 78^{+8}_{-8}]$	$[65^{+3}_{-3}, 77^{+4}_{-4}]$	0.00	0.00
HD 20794 e	6.00	0.51	0.02	27.10	$[59^{+12}_{-11}, 87^{+13}_{-14}]$	$[63^{+11}_{-10}, 87^{+13}_{-16}]$	$[82^{+3}_{-4}, 93^{+2}_{-6}]$	0.50
HD 180617 b	5.91	0.34	0.05	16.50	$[67^{+10}_{-9}, 89^{+11}_{-14}]$	$[60^{+14}_{-8}, 86^{+14}_{-14}]$	$[82^{+4}_{-4}, 94^{+3}_{-9}]$	0.00
HD 210277 b	21.30	1.13	1.49	26.30	$[59^{+5}_{-4}, 70^{+14}_{-3}]$	0.00	0.00	0.00
GJ 887 b	3.29	0.07	0.01	25.20	$[66^{+10}_{-5}, 96^{+7}_{-11}]$	$[85^{+2}_{-2}, 93^{+1}_{-2}]$	0.00	0.00